Chapter 4

Bar Diagnostics in Edge-On Spiral Galaxies. II. Hydrodynamical Simulations

Abstract

We develop diagnostics based on the gas kinematics to identify the presence of a bar in an edge-on spiral galaxy and determine its orientation. We use position-velocity diagrams (PVDs) obtained by projecting edge-on two-dimensional hydrodynamical simulations of the gas flow in a barred galaxy mass model. We show that when a nuclear spiral is formed, the presence of a gap in the PVDs, between the signature of the nuclear spiral and that of the outer parts of the disk, reliably indicates the presence of a bar. This gap is due to the presence of shocks and inflows in the simulations, leading to a depletion of the gas in the main and outer bar regions. If no nuclear spiral signature is present in a PVD, only indirect arguments can be used to argue for the presence of a bar. The shape of the signature of the nuclear spiral, and to a lesser extent that of the outer bar region, allows us to determine the orientation of the bar with respect to the line-of-sight. The presence of dust can also help to discriminate between viewing angles on either side of the bar. Simulations covering a large fraction of parameter space allow us to constrain the bar properties and mass distributions of observed galaxies. The strongest constraint comes from the presence or absence of the signature of a nuclear spiral in the PVD.

4.1 Introduction

The importance of bars in the structure of spiral galaxies is recognised in the Hubble sequence for the classification of galaxies (Sandage 1961). Theoretical

studies of barred spiral galaxies branched early-on in a few directions, each providing insight into an aspect of barred galaxy structure. Studies of resonances and periodic orbits (see e.g. Contopoulos 1980; Contopoulos & Papayannopoulos 1980) provided a basic understanding of the general morphology and structure of barred spirals. Hydrodynamical simulations, either treating the gas as a collection of particles (e.g. Schwarz 1981; Combes & Gerin 1985) or as a continuous medium (e.g. Sanders & Huntley 1976; van Albada 1985), aimed to understand the particular distribution and kinematics of the gaseous component of barred galaxies, taking into account the effects of collisions and/or dissipation. N-body simulations, in most cases self-consistent, modelled the distribution and kinematics of the dominating stellar component of spirals (e.g. Combes & Sanders 1981; Sellwood 1981). These different approaches persist today but they are highly complementary (see e.g. Sellwood & Wilkinson 1993).

In Chapter 3, we highlighted the difficulties involved in the identification of bars in edge-on spiral galaxies. It is clear that the detection of such bars based on photometric or morphological criteria (e.g. de Carvalho & da Costa 1987; Hamabe & Wakamatsu 1989) is uncertain. Kuijken & Merrifield (1995; see also Merrifield 1996) were the first to show that the particular kinematics of barred disks could be used to identify bars in edge-on spirals. They showed that the periodic orbits in an edge-on barred galaxy produce characteristic double-peaked line-of-sight velocity distributions, which can be taken as the signature of a bar. In Chapter 3, we improved on the work of Kuijken & Merrifield (1995). We studied the signatures of individual periodic orbit *families* in the position-velocity diagrams (PVDs) of edge-on spirals (before combining them to model real galaxies), and examined how the PVDs depend on the viewing angle. We adopted a widely used mass model and a well-defined method to populate the orbits. Our aim was to provide insight into the projected kinematical structure of barred disks, and to provide guidance for interpreting stellar and gaseous kinematical observations of edge-on spirals.

We showed in Chapter 3 that the global appearance of a PVD can be used as a diagnostic to detect the presence of a bar in an edge-on disk. The signatures of the various periodic orbit families leave gaps in the PVDs which are a direct consequence of the non-homogeneous distribution of orbits in barred spiral galaxies. The signature of the x_1 periodic orbits is parallelogram-shaped and occupies all four quadrants of the PVDs, reaching very high radial velocities when the bar is seen end-on and only low velocities when the bar is seen side-on. The signature of the x_2 orbits, when present, is similar to that of the x_1 but reaches its maximum radial velocities at opposite orientations. Those features can be used to determine the viewing angle with respect to the bar in an edge-on disk. However, even if carefully chosen and populated, periodic orbits provide only an approximation to the structure and kinematics of the stellar and gaseous components of spiral

galaxies. For example, a number of stars can be on irregular orbits, and no shock can develop.

In this chapter, we concentrate on developing bar diagnostics in edge-on disks using the gaseous component alone. We use the simulations of Athanassoula (1992b; hereafter A92b), designed to study the gas flow and shock formation in barred spiral galaxies. Unlike Chapter 3, these simulations properly take into account the fact that the gas is not a collisionless medium. The shocks and inflows which develop in the simulations lead to better bar diagnostics than those of Chapter 3. In addition, we run simulations covering a large fraction of the parameter space likely to be occupied by real galaxies. The PVDs produced can thus be directly compared with observations not only to detect the presence of bars in edge-on spiral galaxies, but also to constrain the mass distribution of the systems observed. In particular, in Chapter 5, we will apply those diagnostics to long-slit spectroscopic observations of a large sample of edge-on spiral galaxies, most of which have a boxy or peanut-shaped bulge. Our hope is to determine the formation mechanism of these objects and to study the vertical structure of bars. In Paper III, we will develop similar bar diagnostics for the stellar (collisionless) component of barred spiral galaxies, using fully self-consistent three-dimensional N-body simulations.

We describe the mass model and hydrodynamical simulations used in this chapter in § 4.2. In § 4.3, we study the signatures in the PVDs of the various components present in the simulations, and we develop bar diagnostics for edge-on disks. The influence of the parameters of the mass model are also discussed. The effects of dust extinction are illustrated in § 4.4, and we discuss the limitations of our models for the interpretation of real data in § 4.5. We conclude in § 4.6 with a brief summary of our main results.

4.2 Hydrodynamical Simulations

For the hydrodynamical simulations, we use the flux-splitting second-order scheme of G. D. van Albada (van Albada & Roberts 1981; van Albada, van Leer, & Roberts 1982; van Albada 1985). It is the same code as that used by A92b so we will only briefly review its main properties here.

The simulations are two-dimensional (infinitely thin) and time-dependent, and the gas is treated as ideal, isothermal, and non-viscous. We do not consider the self-gravity of the gas, so the flow is calculated using the potential described in Chapter 3 (see also Athanassoula 1992a; hereafter A92a). The mass model has two axisymmetric components, a Kuzmin/Toomre disk (Kuzmin 1956; Toomre 1963) and a bulge-like spherical density distribution. They combine to yield a flat rotation curve in the outer parts of the disk. We use a homogeneous ($n = 0$)

or inhomogeneous ($n = 1$) Ferrers spheroid (Ferrers 1877) as a third component representing the bar. Each model is described by four main parameters: the bar axial ratio a/b, the bar quadrupole moment Q_m (proportional to the mass of the bar), the Lagrangian radius r_L (the radius of the Lagrange points L_1 and L_2 on the major axis of the bar), and the central concentration ρ_c. We recall that the bar semi-major axis is fixed at $a = 5$ kpc, but refer the reader to A92a and Chapter 3 for a more detailed discussion of the mass model.

The simulations are started with a massless bar and an additional axisymmetric component of mass equal to that of the desired final bar. Mass is transfered from that component to the bar over 10^8 yr and the simulations are run until the gas flow is roughly stationary in the frame of reference corotating with the bar (about 10 bar revolutions). An 80×160 cells grid is used to cover a disk of 16 kpc radius, assuming bisymmetry. The inner half of the simulations is then regridded to the 80×160 grid, and the simulations continued for another 5 bar revolutions using this increased spatial resolution (0.1×0.1 kpc^2 cell size; see van Albada & Roberts 1981). Because we only analyse simulations which have reached a steady state, the path of the fluid elements coincide with the streamlines considered in this chapter. Star formation and mass loss are modelled crudely. The gas density is lowered artificially in high density regions and gas is added uniformly over the grid. This process is governed by the equation

$$d\rho_g/dt = \alpha\rho_{g,init}^2 - \alpha\rho_g^2, \tag{4.1}$$

where ρ_g is the gas density, α is a constant (set to 0.3 $M_\odot^{-1}$ pc^2 Gyr^{-1} in most runs), and $\rho_{g,init} = 1 M_\odot$ pc^{-2} is the uniform initial gas density. It therefore takes about 3 Gyr for the gas to be reprocessed.

As in Chapter 3, the models considered are those of A92a (see her Table 1). We will also use her units: 10^6 $M_\odot$ for masses, kpc for lengths, and km s^{-1} for velocities. It is essential to understand the orbital structure of the models to interpret properly the results of the simulations. Orbital properties have been discussed in A92a and Chapter 3, but also in Athanassoula et al. (1983), Papayannopoulos & Petrou (1983), Teuben & Sanders (1985), and others. Here, we will mainly use A92a and Chapter 3 for comparison. We will also draw heavily on the results of A92b, who used the same set of simulations but for different purposes.

4.3 Bar Diagnostics

4.3.1 Detecting Edge-On Bars

The main goal of Chapter 3 and of this chapter is to develop kinematical bar diagnostics in edge-on spiral galaxies, in order to remedy the inadequacies of an

identification based exclusively on the light distribution of the objects. Our main tool is the PVDs, representing the projected density of material in the edge-on disks as a function of line-of-sight velocity and projected position along the major axis (see also Kuijken & Merrifield 1995; Merrifield 1996). In distinction to Chapter 3, where we had to choose a simple method to combine the families of periodic orbits and model the gas distribution of real galaxies, the present hydrodynamical simulations inherently produce the gas density and velocities simultaneously, so that the "right" orbits are naturally populated. The PVDs produced in this chapter can therefore be directly compared with emission line spectroscopic observations of edge-on spiral galaxies (long-slit spectroscopy, Fabry-Perot observations, radio synthesis line-imaging, etc...).

The PVDs presented were obtained by projecting the simulations edge-on and observing them from various viewing angles. Since we are mostly interested in the bar region, we use only the inner 8×8 kpc^2 of the simulations, covered by the high resolution grid. Because the force of the bar decreases steeply with radius, the motion of the gas at large radii can, to first order, be considered circular, and including the outer region would make no difference to our PVDs.

In this section, we will concentrate on understanding the PVDs of two inhomogeneous bar models which are prototypes of models with and without inner Lindblad resonances (ILRs). As suggested in A92a, we will identify the existence and position of the ILRs with the existence and extent of the x_2 periodic orbits. The two models considered are the same as in Chapter 3: model 001 ($a/b = 2.5$, $Q_m = 4.5 \times 10^4$, $r_L = 6.0$, $\rho_c = 2.4 \times 10^4$) and model 086 ($a/b = 5.0$, $Q_m = 4.5 \times 10^4$, $r_L = 6.0$, $\rho_c = 2.4 \times 10^4$). We will then extend our results to other models and analyse how the bar diagnostics developed vary as the parameters of the mass model are changed.

4.3.2 Model 001 (ILRs)

Figure 4.1 shows the face-on surface density of the gas and PVDs for model 001, which has ILRs. Unlike the models of Chapter 3, which are symmetric about both the minor and major axes of the bar, the present simulations are only bisymmetric, so we need to cover a viewing angle range of 180°. The viewing angle ψ is defined to be 0° for a line-of-sight parallel to the major axis of the bar and 90° for a line-of-sight perpendicular to it, increasing counterclockwise in the surface density plots.

As was shown in A92b (see Fig. 2 of that paper, or the surface density plot in Fig. 4.1), there is very little gas in the main and outer bar regions. The two strong parallel narrow segments represent offset shocks on the leading sides of the bar, displaying strong density enhancements, sharp velocity gradients, and

Figure 4.1: Gas distribution and position-velocity diagrams of model 001. The upper-left plot shows the face-on logarithmic gas surface density of the simulation. We use logarithmic values (for the density distribution alone) because the dynamic range of the gas surface density is high. Dark shades denote low density regions. The bar is at 45° to the horizontal, has a semi-major axis length of 5 kpc, and is rotating clockwise. The size of the box is 8×8 kpc^2. The other plots show position-velocity diagrams (projected density of material as a function of line-of-sight velocity and projected position along the major axis) of the gas when the simulation is viewed edge-on. For those plots, dark shades denote high density regions. The angle between the line-of-sight and the bar is indicated in the top-left corner of each diagram, a viewing angle of $\psi = 0°$ indicating that the bar is seen end-on (line-of-sight parallel to the bar) and a viewing angle of $\psi = 90°$ indicating that the bar is seen side-on (line-of-sight perpendicular to the bar). The viewing angle increases counterclockwise in the surface density plots.

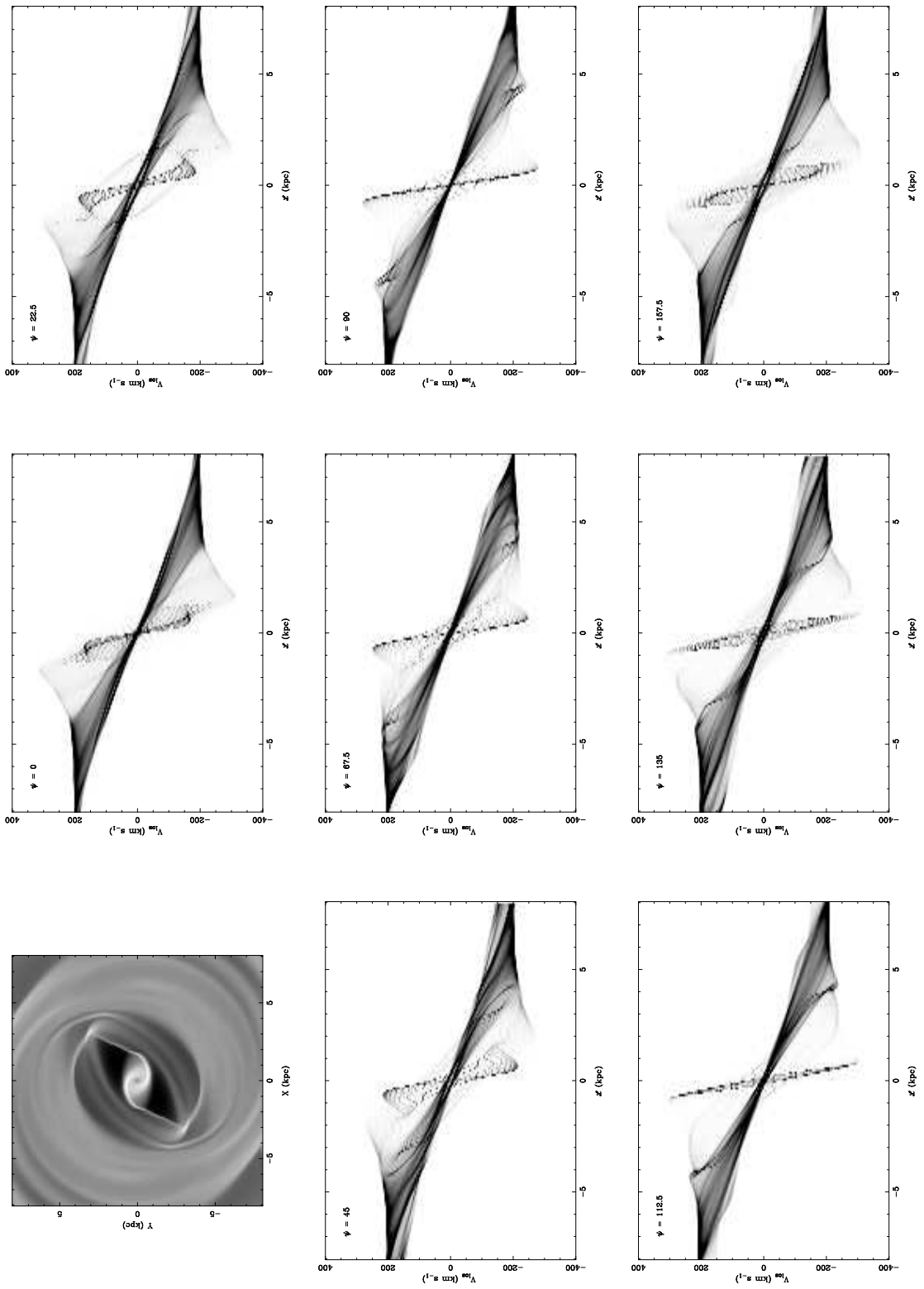

Figure 4.1: *See caption previous page.*

regions of high shear (A92b). They can be identified with the dust lanes observed in barred spiral galaxies. Strong density enhancements can also be seen at the ends of the bar major axis, roughly perpendicular to it. In the inner parts of the bar is a very intense two-armed "nuclear spiral", connecting with the offset shocks. Outside the bar region, the surface density is almost featureless; only a few spiral arms segments are seen. In the outer bar region, the streamlines have roughly the shape and the orientation of the x_1 periodic orbits. As one moves inward, the streamlines change gradually to the shape and orientation corresponding to the x_2 periodic orbits. This flow pattern leads to the offset shocks and results in an inflow of gas toward the nuclear region, accounting for the gas distribution in the bar: low densities in the main and outer parts of the bar, and high densities in the center (A92b). As we already mentioned, the flow is almost circular outside the bar region.

The PVDs in Figure 4.1 show the existence of three distinct regions: an inner region, corresponding to the nuclear spiral; an intermediate region, corresponding to the main and outer parts of the bar; and an external region, corresponding to the region outside the bar. It is important to notice how low the density of the intermediate region is, compared to that in the other two regions. This is no surprise since, as mentioned in A92b and above, most of the bar region has very low gas density, with the exception of the central region and the two shock loci. Let us now examine each of the three regions separately, by keeping only the gas in the targeted region (and masking out the gas in the other regions) when calculating the PVDs.

Figure 4.2 shows the surface density and PVDs of model 001 when considering the low density main and outer bar regions only. Because the high density regions have been masked out and because we are looking only at relatively low density regions, we see much more structure in the PVDs of Figure 4.2 than in the corresponding sections of the PVDs of Figure 4.1.

To see what the various components of the gas density contribute to the PVDs, we have also masked out all areas except for the shock loci along the leading sides of the bar, or the density enhancements near the ends of the bar major axis (not shown). The gas in the shock loci does not contribute any very outstanding features to the PVDs, the main reason being that the amount of gas integrated along most lines-of-sight is small, since the features are very narrow. At $\psi = 22.5°$, when the line-of-sight is parallel to the shock loci, they contribute the two linear segments which separate the "dark" and "light" regions of the PVD slightly inside $L = \pm 2$. The high density enhancements near the ends of the bar major axis contribute the very strong straight line segments going through the center at $\psi = 0°$ and $22.5°$. For these angles, they are seen roughly as segments of circles. For viewing angles near $90°$, they give rise to the undulating parts of the PVDs

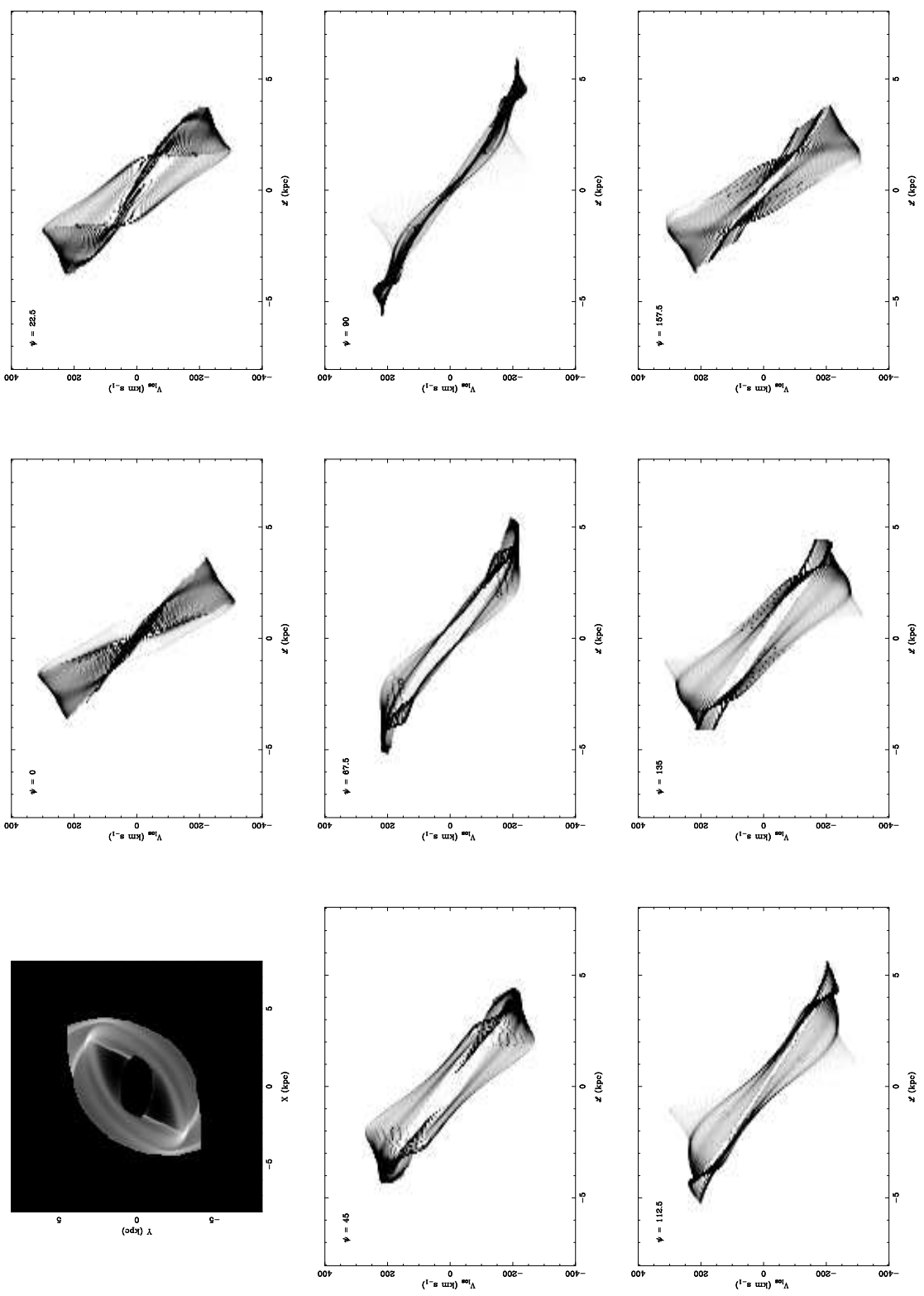

Figure 4.2: Same as Figure 4.1 but for the low density main and outer bar regions of model 001 only.

at large radii.

When compared with Figure 3.4, Figure 4.2 shows, at first glance, many similarities, but also, when scrutinised more closely, a number of differences. This could be expected since the gas streamlines follow loosely, but not exactly, the shape and orientation of the x_1 orbits, which are elongated parallel to the bar.

The parallelogram-shaped signature of the x_1 orbits in Figure 3.4 is again observed here and the "forbidden" quadrants are again populated. This is due to the fact that both the x_1 orbits and the streamlines in the main and outer bar regions are not circular, but elongated. In the gas, however, the parallelogram shape is also present for $\psi = 0°$, while the PVD of the x_1 orbits showed a bow-shaped feature. The reason is that, unlike the x_1 orbits, the streamlines do not have their major axes parallel to that of the bar, but rather at an angle of about 20° to it (see A92b). Also, at $\psi = 90°$, the x_1 orbits show a near-linear PVD, while the gas shows an additional faint bow-shaped feature near the center (the feature is visible for $67.5° \lesssim \psi \lesssim 135°$). Masking a larger fraction of the simulation (not shown), it is possible to show that the extra feature, which reaches high radial velocities, arises from the very low density regions just inside the offset shocks, close to the major axis of the bar. In this section of the bar region, the flow differs substantially from the behaviour of the x_1 periodic orbits.

The elongated "hole" in the center of the PVDs, seen at intermediate viewing angles, is present in both sets of PVDs, and is due to the way the x_1 orbit family was terminated and the way the gas density was masked. This causes in both cases an absence (or low-density) of quasi-circular streamlines near the end of the bar.

For $\psi = 0°$, the maximum velocity in the PVD occurs near the center; for $\psi = 90°$, it occurs at the largest radii. This was also found for the PVDs of the x_1 orbits in Chapter 3, where it was explained by considering the trace of an elongated orbit in a PVD as a function of the viewing angle and (average) distance from the center. The explanation is analogous here. Because the streamlines in the main and outer bar regions become more elongated with decreasing radius, the envelope of their signature in the PVDs increases rapidly with decreasing projected distance for viewing angles close to 0°/180°, and decreases with decreasing projected distance for viewing angles close to 90° (the streamlines are elongated parallel to the bar in those regions). We refer the reader to Chapter 3 for a fuller explanation. There is also a reduced degree of symmetry with respect to the viewing angles 0° and 90°, in particular as far as the angles 67.5° and 112.5° are concerned. They are, of course, identical in the periodic orbits PVDs of Chapter 3. This is because the flow is strongly bisymmetric, as opposed to being almost symmetric with respect to both axes of the bar (see Fig. 2 of A92b).

In Figure 4.2, we see that the radial velocities are maximum (compared to

the circular velocity) for lines-of-sight almost parallel to the bar (highest values for 0° and 157.7°), and decrease as ψ increases, to reach a minimum when the line-of-sight is roughly along the bar minor axis (lowest values for 90° and 67.5°). This was to be expected since, like the x_1 orbits, the streamlines in the main and outer parts of the bar are elongated parallel to it. Similarly, the position where the maximum occurs moves out as the viewing angle increases from $\psi = 0°$ to $\psi = 90°$ (see above). However, the maxima generally occur at a larger distance from the center than in the case of the x_1 orbits (this is easily seen by comparing Fig. 3.4 and 4.2). This is due to the fact that the x_1-like flow does not extend up to the center of the hydrodynamical simulation, contrary to the x_1 periodic orbits of Chapter 3, but is truncated at a certain radius. For example, the nuclear spiral, which has an x_2-like behaviour, extends to about 1.6 kpc on the bar minor axis, which is exactly the projected distance at which the envelope of the signature of the main bar region drops abruptly for $\psi = 0°$.

We can repeat the masking process to keep only the region of the simulation containing the nuclear spiral, as shown in Figure 4.3. Comparing the PVDs thus obtained with those of the x_2 family of periodic orbits (Fig. 3.5), we again find both similarities and differences. In both cases, we see inverted S-shaped features or near straight segments passing through the center. This is explained by the decrease of the streamlines eccentricity with decreasing radius (see Ch. 3 for a more thorough explanation). More similarity is found if we compare PVDs at viewing angles differing by about 20°, i.e. comparing the gaseous PVD at $\psi = 112.5°$ with the orbital one at $\psi = 90°$. This offset corresponds to the offset of the straight shocks with respect to the major axis of the bar (A92b). Also, the PVDs of the nuclear spiral are more asymmetric with respect to the viewing angles 0° and 90° (e.g. comparing the PVDs at $\psi = 22.5°$ and $\psi = -22.5° = 157.5°$) than the PVDs of the main and outer bar regions. This effect is due to the stronger bisymmetry of the nuclear spiral.

Because the streamlines in the central region are elongated perpendicular to the bar, like the x_2 orbits, higher radial velocities (compared to the circular velocity) are reached when the bar is seen side-on than when the bar is seen end-on. Considering the maximum velocity of the PVDs as a function of the viewing angle, we find that it is highest for $\psi = 112.5°$ and 135° and lowest for $\psi = 0°$ and 22.5°, in agreement with the offset mentioned above. The "hole" in the parallelogram-shaped signature of the x_2 orbits (see Fig. 3.5) has completely disappeared in the hydrodynamical simulation, because the x_2-like behaviour of the gas flow persists past the inner ILR and the flow becomes almost circular in the very center.

Figure 4.4 isolates the signature of the region outside the bar in the PVDs. Because the influence of the bar decreases rapidly with radius, the flow outside the bar is close to circular. A perfectly circular orbit would yield an identical

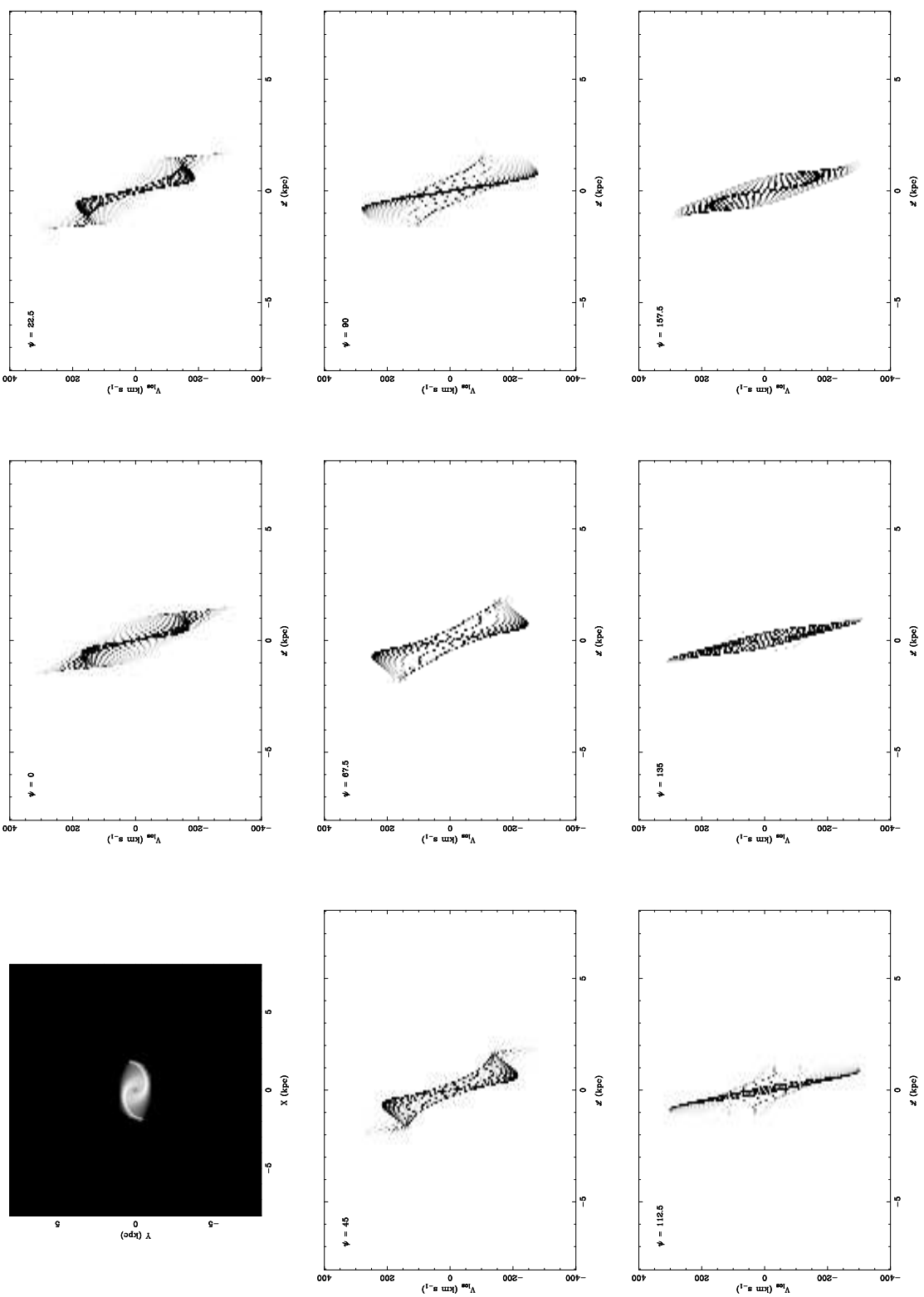

Figure 4.3: Same as Figure 4.1 but for the high density nuclear spiral region of model 001 only.

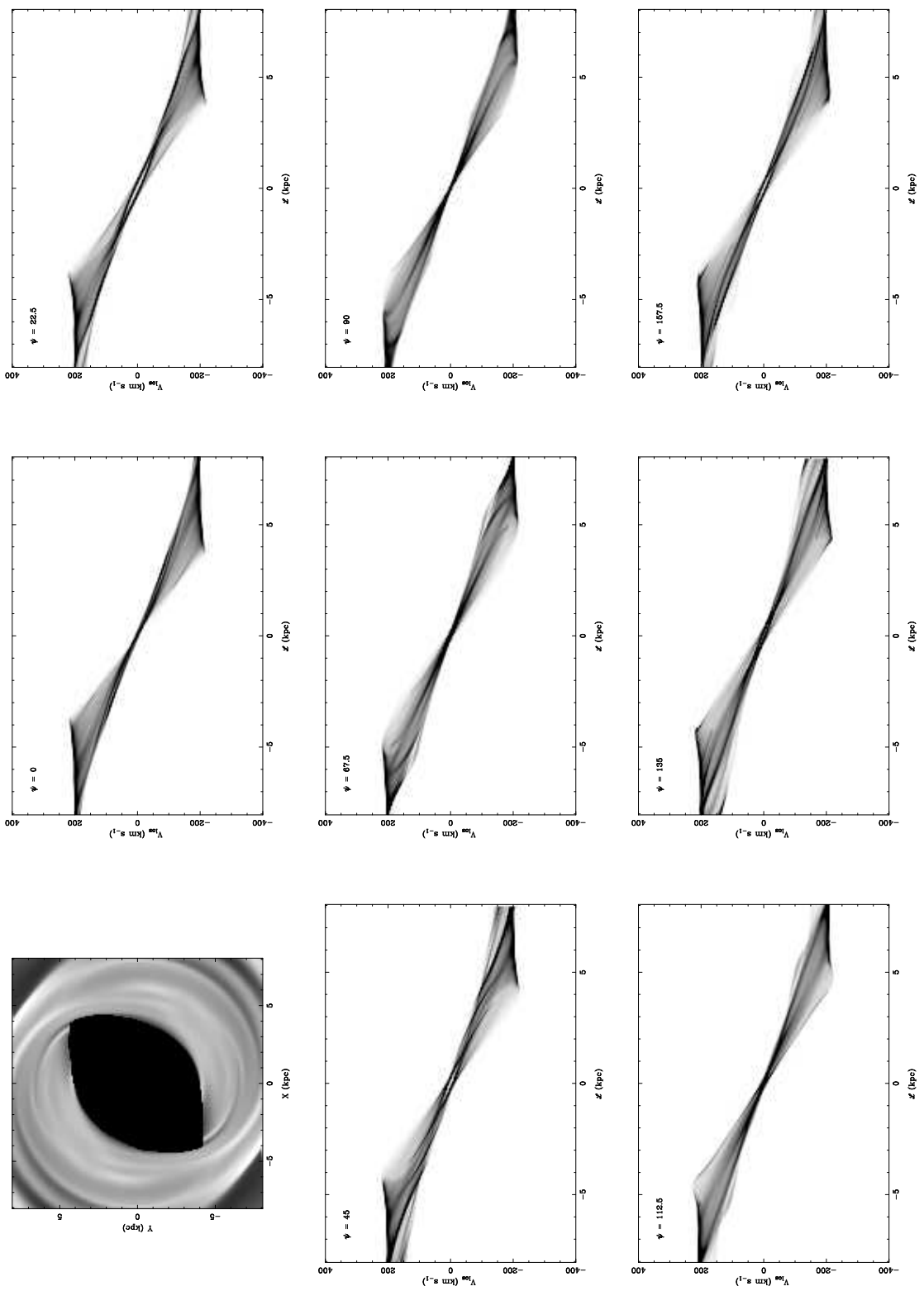

Figure 4.4: Same as Figure 4.1 but for the high density outer regions of model 001 only.

inclined straight line passing through the origin in all PVDs. The structure seen here can thus be thought of as a succession of near-circular orbits of increasing radii, yielding the "bow tie" signature observed. The "hole" seen in the center of the PVDs at certain viewing angles (e.g. $\psi = 45°$) is again due to the fact that the orbits are not perfectly circular (see Fig. 3.6). The strong almost solid-body features forming loop-like structures near the upper and lower limits of the envelope of the signature are due to tightly wound spiral arms in the outer disk.

4.3.3 Model 086 (no-ILRs)

Figure 4.5 shows the face-on surface density distribution of model 086, which has no ILRs (or, equivalently, has no x_2 periodic orbits), and the PVDs obtained using an edge-on projection. The main difference from the density distribution of model 001 is the absence of any significant nuclear spiral. The strong straight and narrow features in the center of the bar are centered shocks, caused by the high curvature of the streamlines near the major axis of the bar (see Fig. 4 in A92b). Similarly, the x_1 orbits in this model have high curvatures or loops near their major axes. The shock loci do not curve near the center because no streamlines perpendicular to the bar exist; there are no x_2 periodic orbits in this model. The shocks, however, still drive an inflow of gas, resulting in the *entire* bar region being gas depleted. As expected, the region outside the bar is almost unaffected by the change in the bar axial ratio compared to model 001.

The PVDs in model 086 reflect all of the above properties. In particular, they lack the central feature associated with the nuclear spiral in model 001, and the signature of the main and outer bar regions is very faint (Fig. 4.5 should be contrasted with Fig. 4.1). Because of the absence of an x_2-like flow in the central region of the simulation, the x_1-like flow extends inward all the way to the center. In good agreement with what happens for the periodic orbits (see Ch. 3 or A92a), the streamlines are also much more eccentric than those of model 001. The parallelogram-shaped envelope of the signature of the main and outer bar regions in the PVDs therefore reaches even more extreme radial velocities (compared to the circular velocity) than in model 001, and the rising part of the envelope extends almost all the way to the center for viewing angles close to $0°/180°$ (see also Fig. 3.9). When the bar is seen close to end-on, radial velocities more than twice those in the outer parts are reached. These velocities decrease rapidly as the viewing angle approaches $\psi = 90°$. As in the case of model 001, the regions outside the bar lead to a strong almost solid-body component in all PVDs.

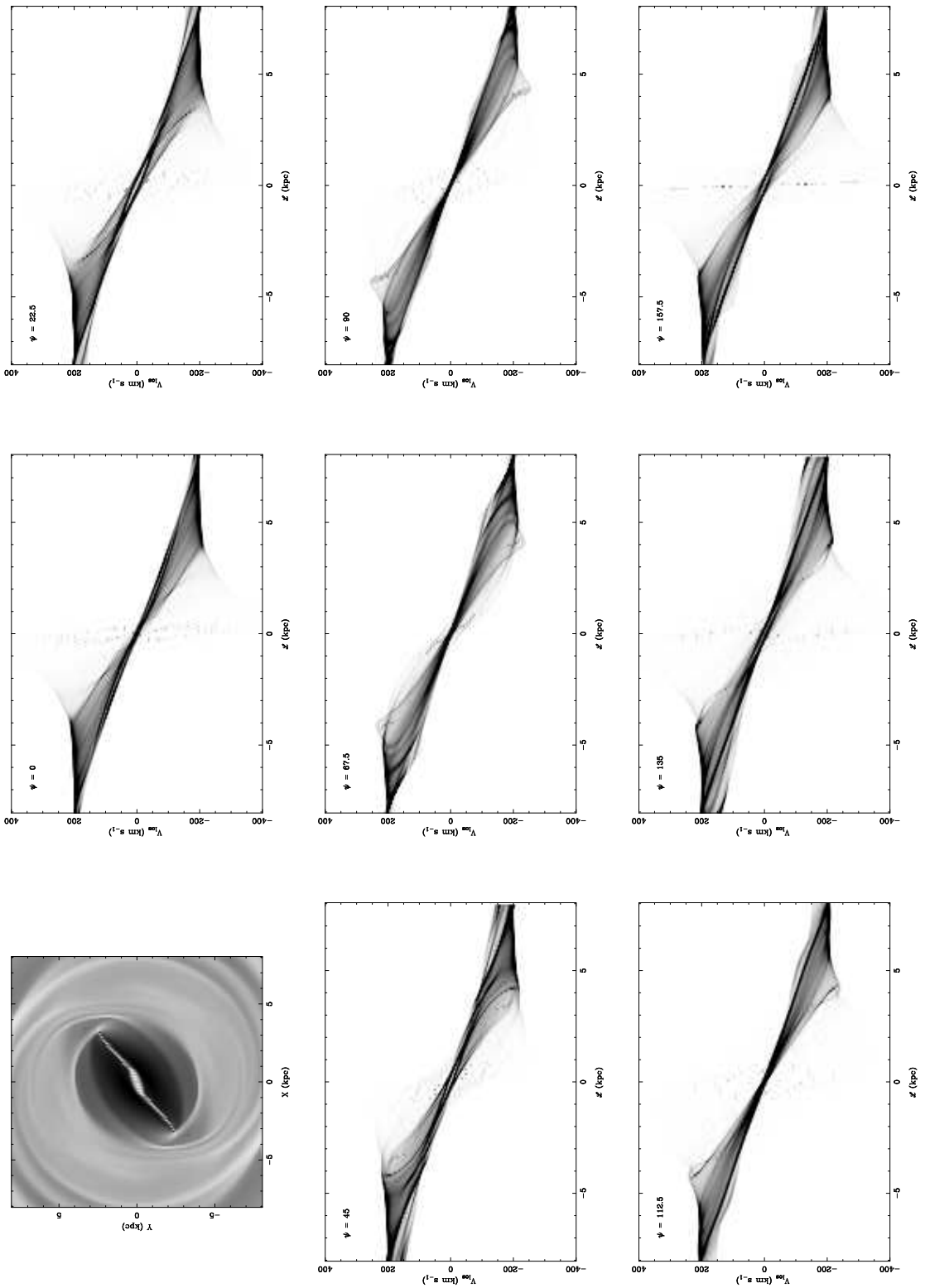

Figure 4.5: Same as Figure 4.1 but for model 086.

4.3.4 Other Models

Now that the general characteristics of the gas flow in models with and without ILRs are understood, it is possible to explore how the gas behaviour changes when the parameters of the mass model are varied. We can hope thereby not only to extend the diagnostics developed to identify bars in edge-on spiral galaxies (and their orientations relative to the line-of-sight), but also to develop criteria allowing us to constrain the bar properties and mass distribution of the systems. To achieve this, we will analyse sequences of simulations corresponding to the ranges along the axes of parameter space likely to be occupied by real galaxies. We will concentrate on understanding the gas flow within the barred region of the simulations, and will use extensively for that purpose the results of A92a and A92b. In particular, A92b showed that nuclear spirals occur in models with an extended x_2 family of periodic orbits and lead to offset shocks, while centered shocks occur in models with no or shortly extended x_2 orbits. She also showed that x_1 periodic orbits with a high curvature near the bar major axis are essential to the formation of shocks, and that such shocks lead to an inflow of gas toward the central region of the simulations, depleting the main and outer bar regions.

Figure 4.6 shows a sequence of simulations with varying bar axial ratio a/b (the other parameters are kept fixed at those of model 001). The figure shows, for each simulation, the face-on surface density distribution and the velocity field (with a few streamlines) in the frame of reference corotating with the bar. It also shows the PVDs obtained for various viewing angles with respect to the bar when the simulation is viewed edge-on. To limit the number of figures, and since there is some degree of symmetry with respect to $\psi = 0°$ and $90°$, we do not show any PVDs with $\psi > 90°$. Nevertheless, such viewing angles were considered, and the corresponding results will be included in the discussion whenever necessary.

For small bar axial ratios, when the effect of the bar is similar to that of an oval distortion and the shocks are short and curved, the main bar region is not strongly gas depleted and its signature is easily visible in the PVDs. As we consider simulations with increasingly higher bar axial ratios, the density in the region of the PVDs which corresponds to the main and outer bar regions drops considerably. It reaches its lowest values for the highest bar axial ratio considered ($a/b = 5$), for which the shock loci are straight and close to the bar major axis.

In Figure 4.6, the envelope of the signature of the main and outer bar regions in the PVDs becomes more extreme as the bar axial ratio is increased: the maximum radial velocities reached for small viewing angles increase and the positions of the maxima get closer to the center. The opposite is true for large viewing angles. This is easily understood because, as the bar axial ratio increases, the eccentricity of the streamlines in the main and outer bar regions (and that of the x_1 orbits, see A92a) also increases, leading to higher velocities along the line-of-sight when

Figure 4.6: Gas distribution and position-velocity diagrams for a sequence of models of increasing bar axial ratio a/b. The models are 010, 005, 001, 083, and 086, with, respectively, $a/b = 1.5$, 2.0, 2.5, 3.0, and 5.0. The other parameters of the models are kept fixed at those of model 001. The first row of plots shows the face-on logarithmic gas surface densities of the simulations. We use logarithmic values (for the density distributions alone) because the dynamic range of the gas surface densities is high. Dark shades denote low density regions. The bar is at 45° to the horizontal, has a semi-major axis length of 5 kpc, and is rotating clockwise. The size of the box is 8×8 kpc^2. The second row of plots shows velocity vectors and gas streamlines in the frame of reference corotating with the bar. The following rows of plots show position-velocity diagrams (projected density of material as a function of line-of-sight velocity and projected position along the major axis) of the gas when the simulations are viewed edge-on. For those plots, dark shades denote high density regions. The angle between the line-of-sight and the bar is indicated in the top-left corner of the first diagram of each row, a viewing angle of $\psi = 0°$ indicating that the bar is seen end-on (line-of-sight parallel to the bar) and a viewing angle of $\psi = 90°$ indicating that the bar is seen side-on (line-of-sight perpendicular to the bar). The viewing angle increases counterclockwise in the surface density plots.

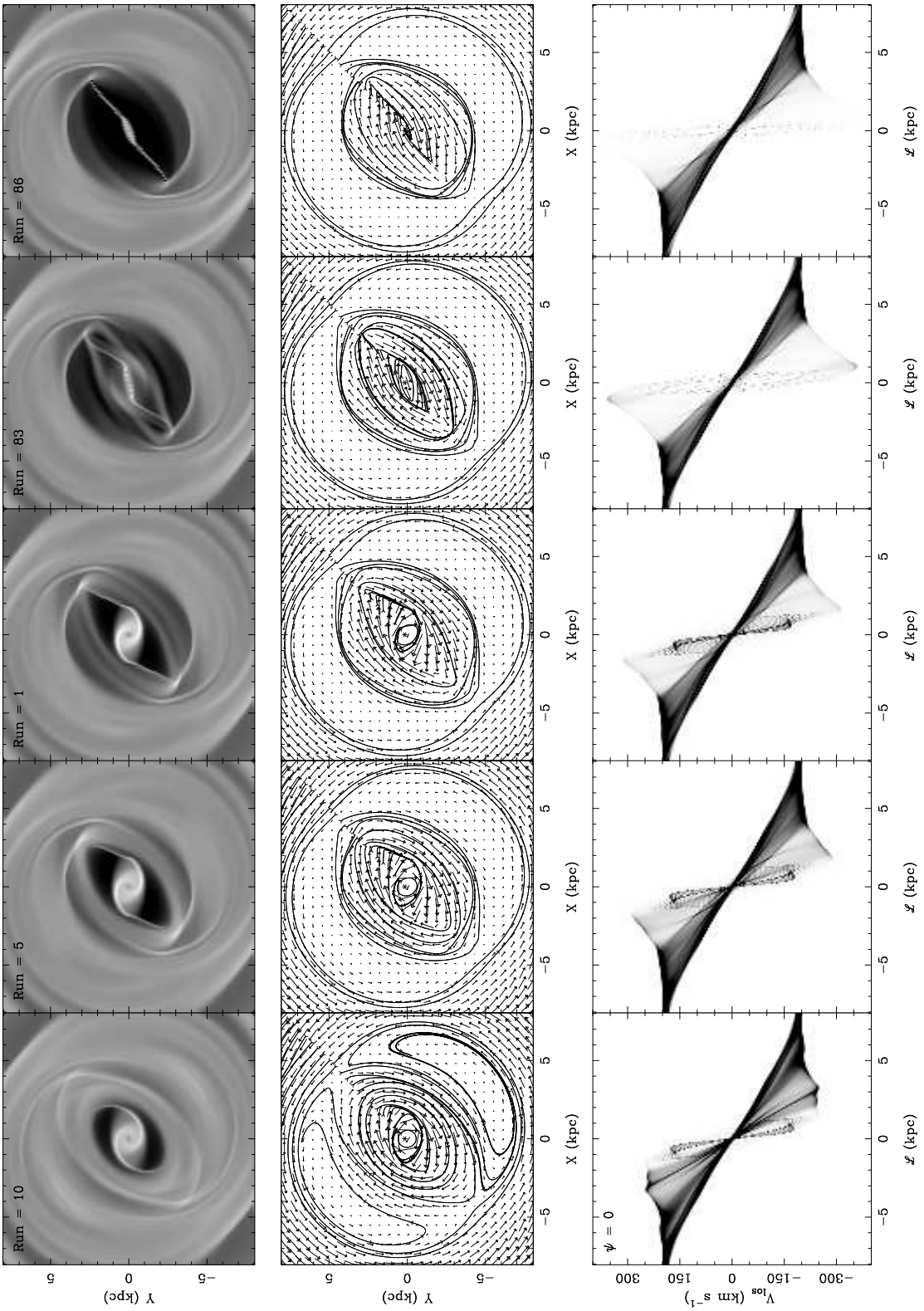

Figure 4.6: *See caption previous page.*

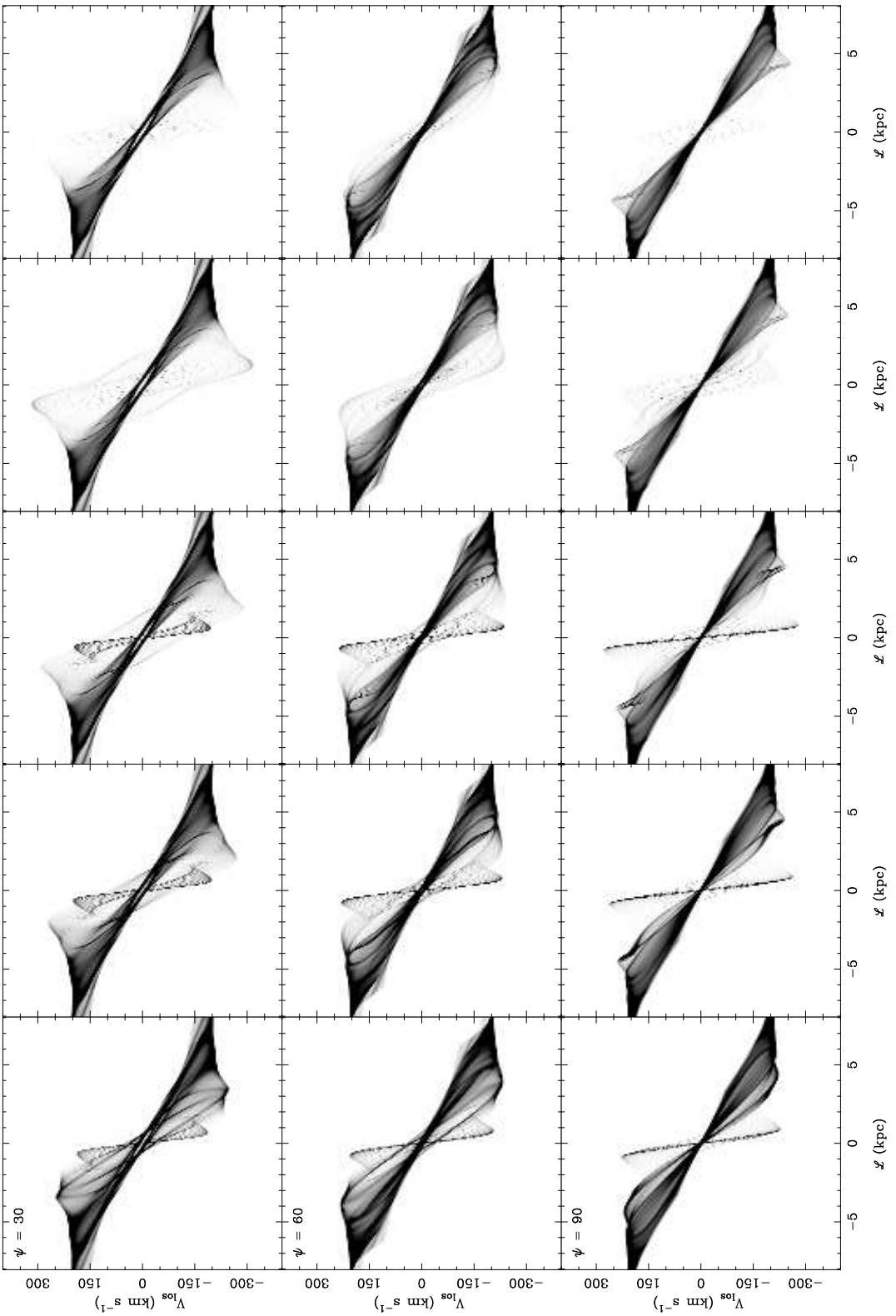

Figure 4.6: *Continued.*

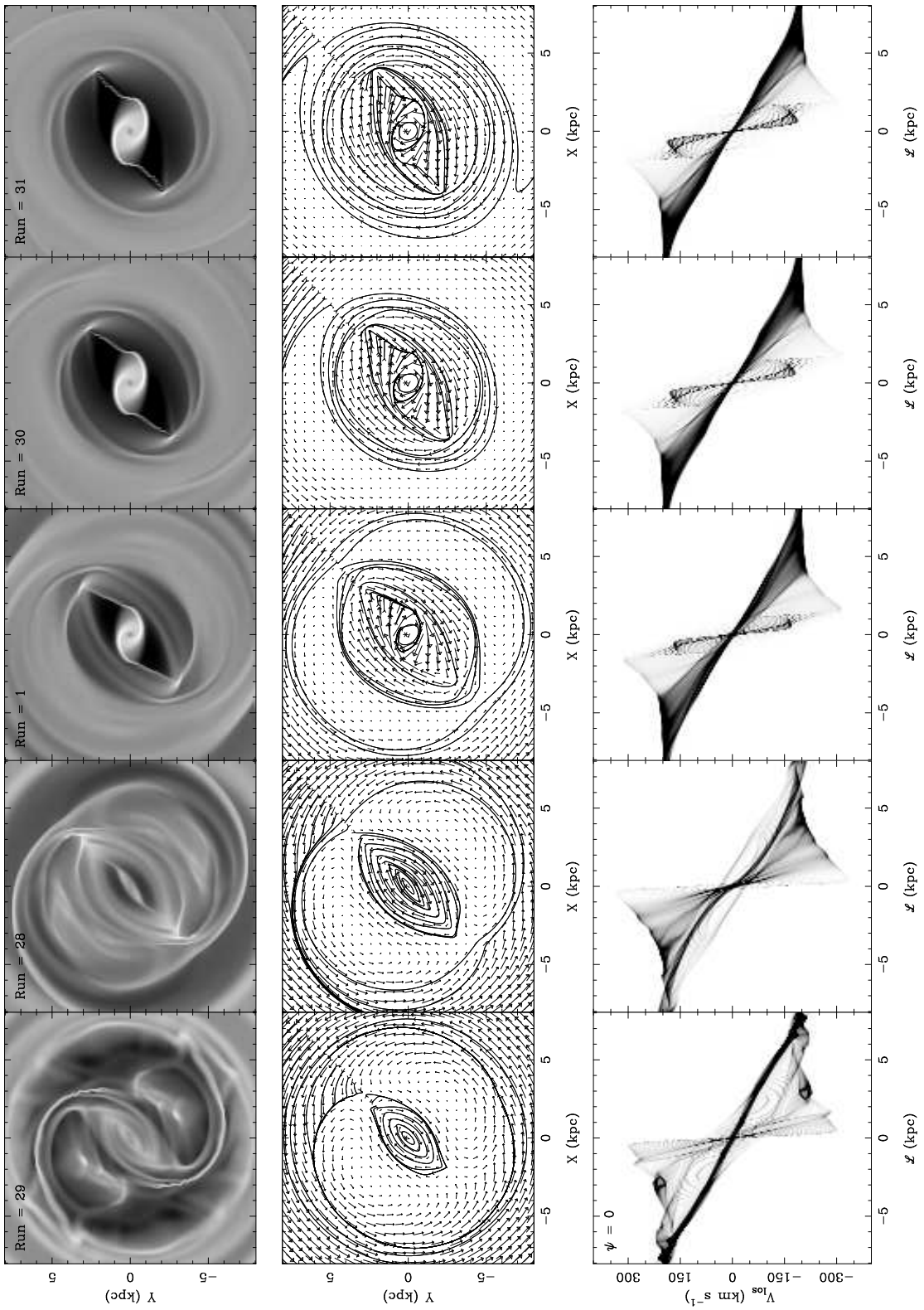

Figure 4.7: Same as Figure 4.6 but for a sequence of models of increasing Lagrangian radius r_L. The models are 029, 028, 001, 030, and 031, with, respectively, $r_L = 4.0$, 5.0, 6.0, 7.0, and 8.0. The other parameters of the models are kept fixed at those of model 001.

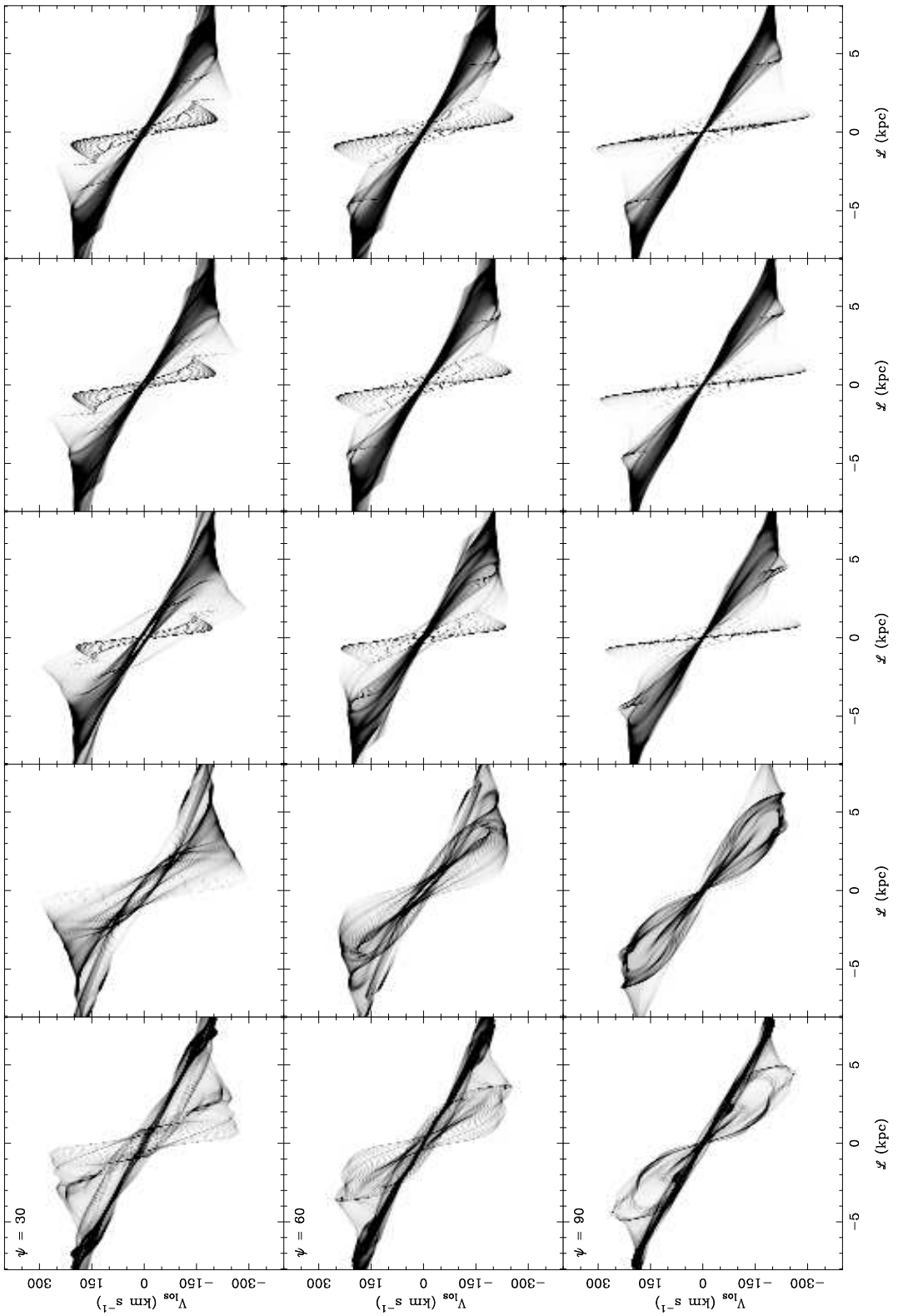

Figure 4.7: *Continued.*

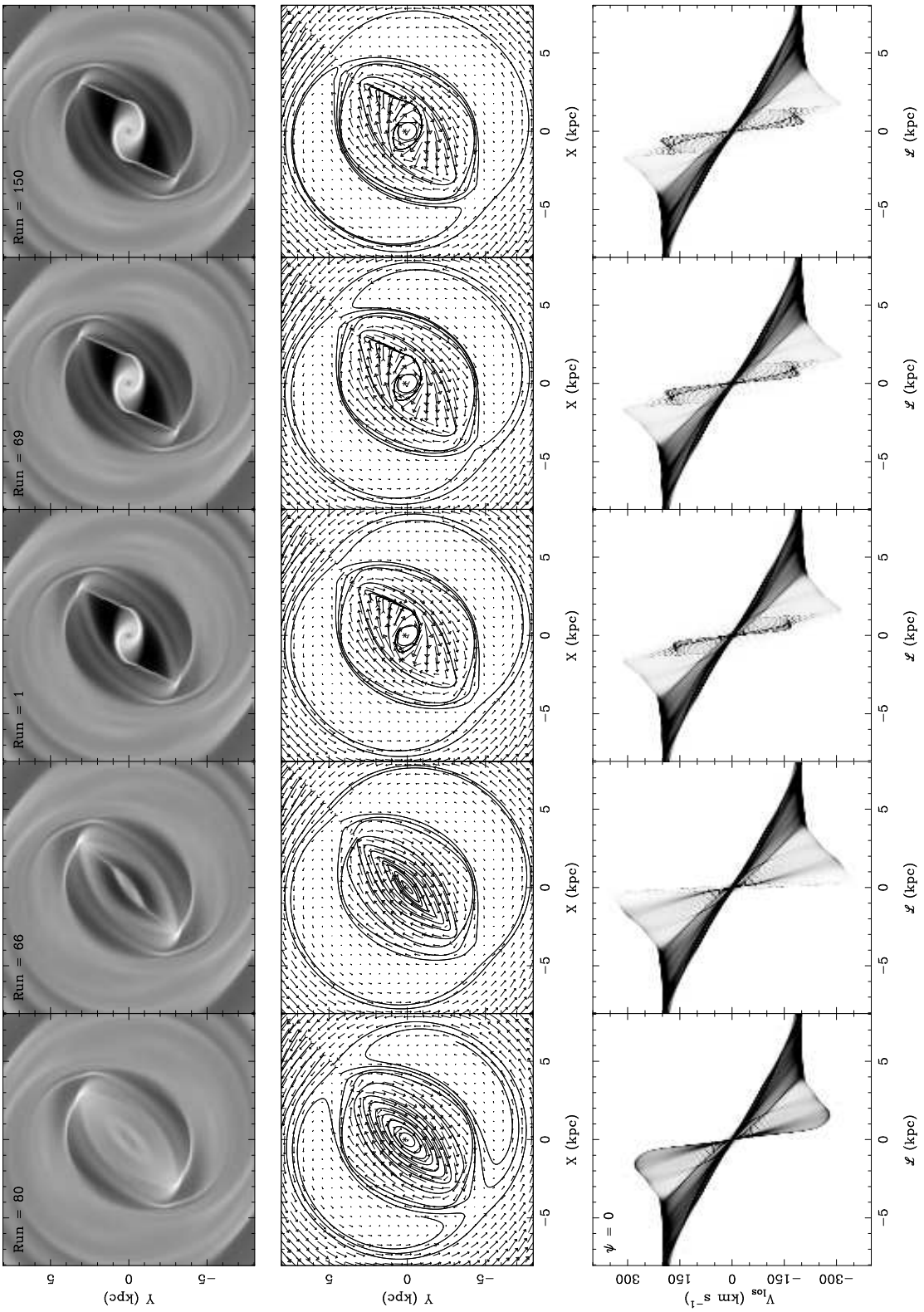

Figure 4.8: Same as Figure 4.6 but for a sequence of models of increasing central density ρ_c. The models are 080, 066, 001, 069, and 150, with, respectively, $\rho_c = 0.4 \times 10^4$, 1.6×10^4, 2.4×10^4, 3.2×10^4, and 4.0×10^4. The other parameters of the models are kept fixed at those of model 001.

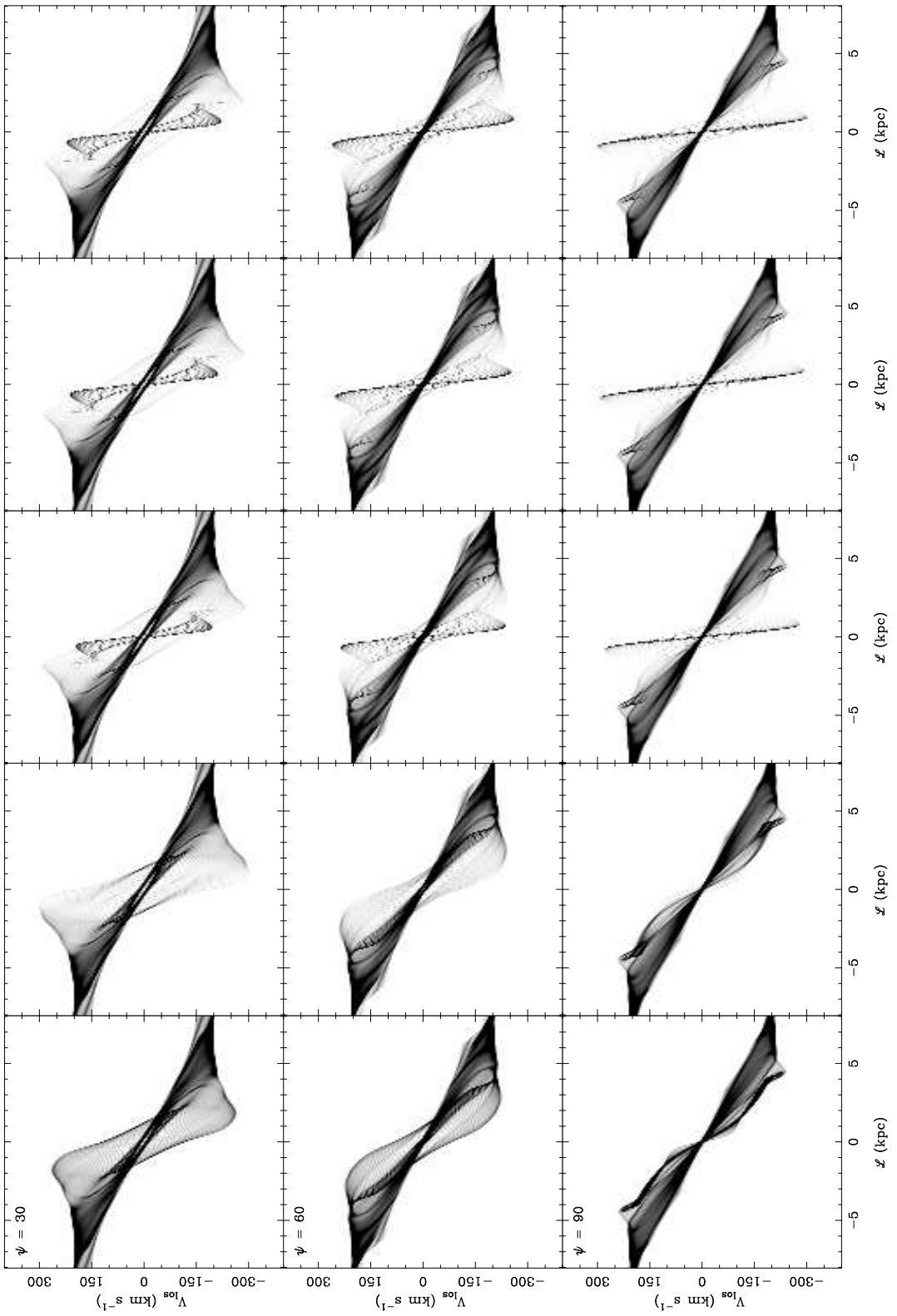

Figure 4.8: *Continued.*

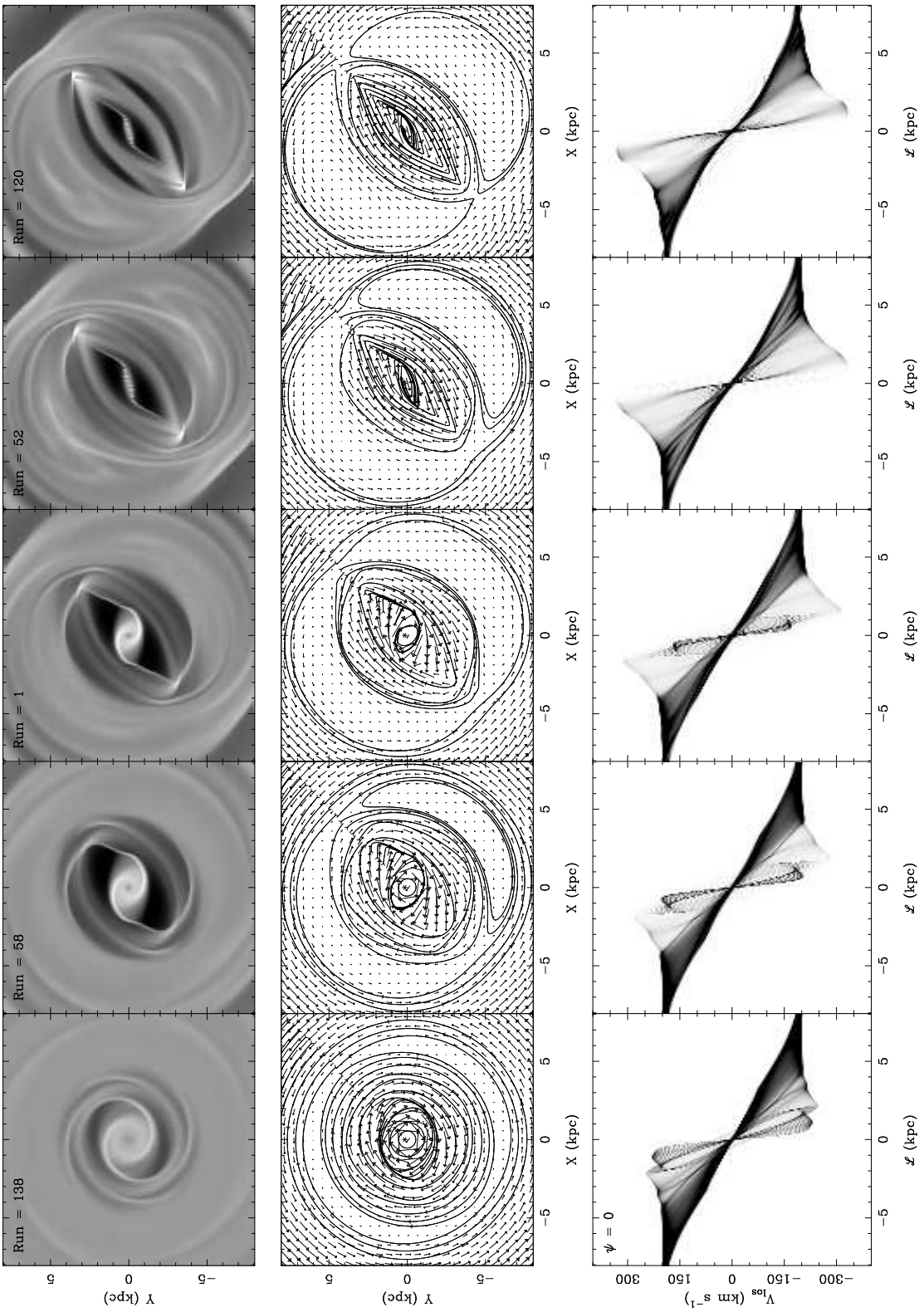

Figure 4.9: Same as Figure 4.6 but for a sequence of models of increasing bar quadrupole moment Q_m. The models are 138, 058, 001, 052, and 120, with, respectively, $Q_m = 0.5 \times 10^4$, 2.5×10^4, 4.5×10^4, 6.0×10^4, and 8.0×10^4. The other parameters of the models are kept fixed at those of model 001.

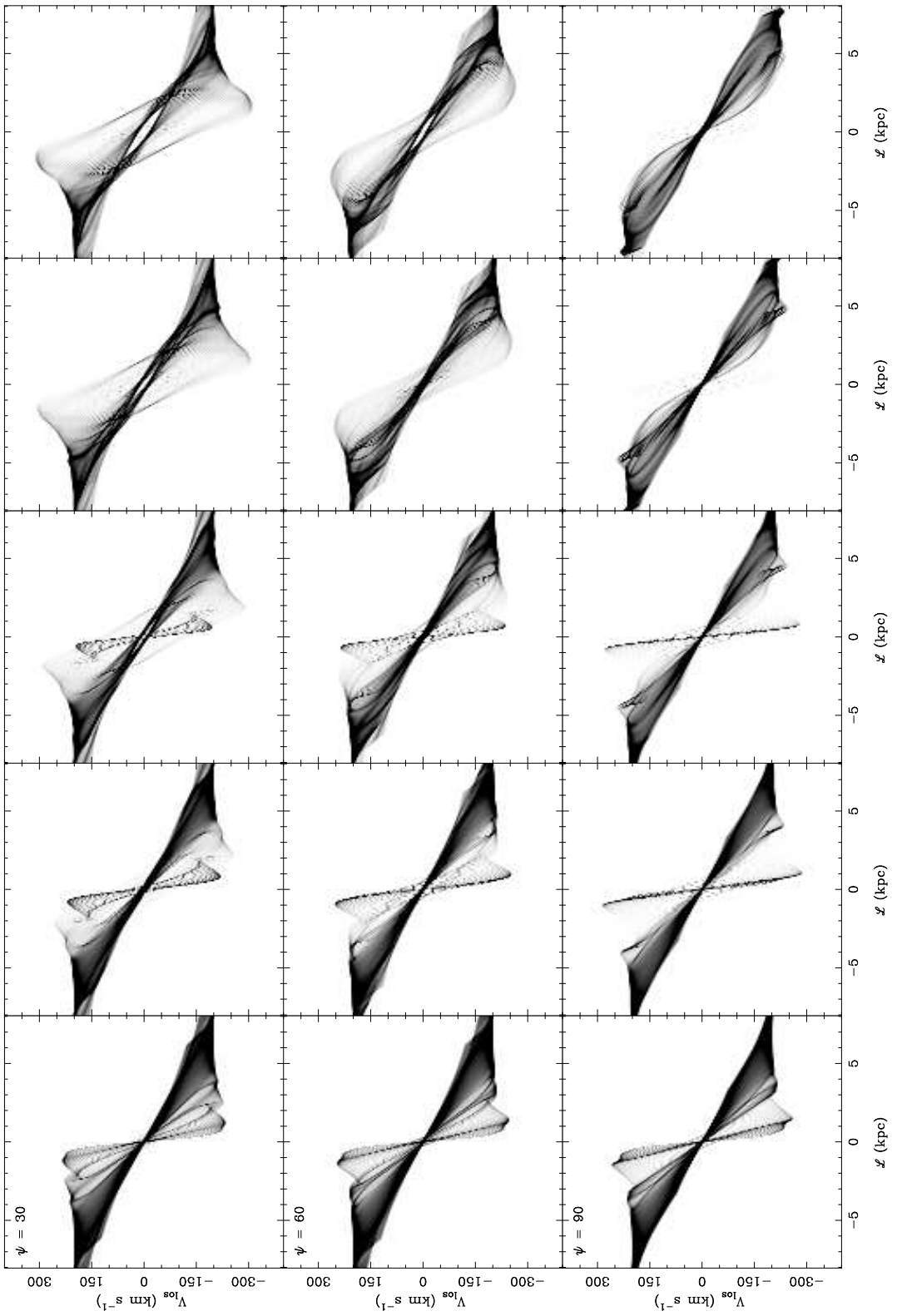

Figure 4.9: *Continued.*

the bar is seen end-on and smaller velocities when it is seen side-on. The most important effect of an increase of the axial ratio of the bar is the disappearance of the nuclear spiral for axial ratios $a/b \gtrsim 2.7$. Because the nuclear spiral is associated with an x_2-like flow, and because the range of radii occupied by the x_2 orbits decreases rapidly as the bar axial ratio is increased (see Fig. 6 of A92a), the nuclear spiral and its associated inverted S-shaped signature in the PVDs disappear for large bar axial ratios. The maximum radial velocity reached by the signature of the nuclear spiral varies little with the bar axial ratio (when present).

Figure 4.7 shows how the gas density and kinematics change when the Lagrangian radius of the mass model is varied. Model 029 is probably unphysical, as the corotation radius (which is almost equal to the Lagrangian radius) would be within the bar. This is very unlikely to happen in a real galaxy, as there would be no x_1 periodic orbits at the end of the bar to support it self-consistently (see, e.g., Contopoulos 1980). A92b showed that the shock loci within the bar are offset toward its leading sides and of the form observed in early-type barred spiral galaxies only for a restricted range of Lagrangian radii, namely $r_L = (1.2 \pm 0.2)a$. All the observational estimates for strongly barred early-type spirals also give values in that range (see, e.g., A92b; Elmegreen 1996). We will thus concentrate on those Lagrangian radii here. Model 028, the limiting case with $r_L = 5.0$, shows strong spiral arms starting at the end of the bar and extending to large radii. The spiral arms are easily identified in the PVDs as long filamentary structures. This model has no nuclear spiral, and thus no corresponding inverted S-shaped feature in the PVDs. This is not the case for models with lower pattern speeds, or, equivalently, larger Lagrangian radii. Those models have extended x_2 periodic orbit families and therefore nuclear spirals (see A92b). As the pattern speed of the bar is decreased, the radial range occupied by the x_2 periodic orbits is increased (A92a), and the nuclear spiral becomes more predominant. The main and outer bar regions decrease accordingly. This effect is clearly seen in the PVDs of Figure 4.7. For increasing Lagrangian radii, they show an increase of the radial extent of the nuclear spiral signature, and a decrease of the radial extent of the signature of main and outer bar regions. There is also an increase of the maximum radial velocity of the x_2 feature, but the effect is rather small.

Figure 4.8 shows the behaviour of the gas as the central concentration of the mass model is varied. For low central concentrations, the gas streamlines are oval and aligned with the bar, there are no shocks, and the barred region is only slightly gas depleted. The signature of the main and outer bar regions in the PVDs is then clear. As the central concentration is increased, the streamlines become more eccentric, and the envelope of the signature of the main and outer bar regions extends further to high velocities. Once the central concentration reaches $\rho_c \approx 2.2 \times 10^4$, an x_2-like flow appears in the center of the bar and a nuclear spiral and offset shocks are formed. These changes are also easily seen in the

PVDs, which acquire an inverted S-shaped feature, while the density in the main and outer bar regions drops. The region occupied by the x_2 orbits then increases with increasing central concentration (A92a), and so does the radial extent of the nuclear spiral signature in the PVDs. An increase in the central concentration of the mass model has similar effects to an increase of the Lagrangian radius (see Fig. 4.7). This is not surprising, since both changes influence the location of the resonances similarly.

Figure 4.9 shows a sequence of simulations with different values of the bar quadrupole moment. For the lowest quadrupole moment, the bar is weak and the flow is close to circular, with only a weak spiral shock in the center. This does no cause substantial inflow, and the gas density in the main and outer bar regions is relatively high. The velocity field shows that there is a transition from a x_1-like flow to a x_2-like flow in the central region, but the effect is not strong since the eccentricity of the streamlines is weak. All these effects reflect themselves in the PVDs. For somewhat higher bar quadrupole moments, the nuclear spiral is well-developed and its signature strong in the PVDs, with a gap present between it and the solid-body signature of the outer parts of the galaxy. As the bar quadrupole moment is increased further, the envelope of the signature of the main and outer bar regions in the PVDs becomes more extreme, reaching higher maximum velocities and extending closer to the center. For $Q_m \gtrsim 5.5 \times 10^4$, the nuclear spiral disappears. Those two effects are due to the fact that the eccentricity of the streamlines increases significantly with increasing bar quadrupole moment, while the region occupied by the x_2 orbits decreases until it disappears completely (see A92a). Because the bar is so strong for high quadrupole moments, the flow is non-circular even in the outer parts of the simulations, and a "hole" is present in the center of the PVDs at intermediate viewing angles. Not surprisingly, the variations in the gas distribution and kinematics are similar when the bar quadrupole moment is increased and when the axial ratio of the bar is increased.

4.4 Dust Extinction

It is interesting to note that the PVDs discussed so far have a limited degree of symmetry with respect to the viewing angles 0° and 90°. This means that although it is relatively easy to determine whether a line-of-sight is close to the major or minor axis of a bar ($|\psi|$), it is considerably harder to determine in which half of the PVD (positive or negative projected distances from the center) the near side of the bar is located ($\pm\psi$).

This situation can be contrasted to that in the Galaxy, where most studies have no difficulty identifying the quadrant in which the near side of the Galactic

bar is located. Studies using infrared photometry (e.g. Dwek et al. 1995; Binney, Gerhard, & Spergel 1997), star counts (e.g. Weinberg 1992; Stanek et al. 1997), gaseous or stellar kinematics (e.g. Binney et al. 1991; Wada et al. 1994; Zhao, Spergel, & Rich 1994; see also Beaulieu 1996; Sevenster et al. 1997), and microlensing events (e.g. Paczynski et al. 1994) all indicate a bar making an angle of 15° to 45° with respect to the line-of-sight to the Galactic center (positive values indicating that the near side of the bar is at positive Galactic longitude). In the case of the Galaxy, at least two effects help the observer determine the exact orientation of the bar. Firstly, projection effects (both in longitude and latitude) mean two lines-of-sight on each side of the Galactic center reach correspondingly different parts of the bar (e.g. Binney et al. 1991). Secondly, the large difference between the distances to each side of the bar means point sources in the far side of the bar will appear significantly fainter than corresponding sources in the near side (e.g. Stanek et al. 1997). In addition, the far side of the bar will appear thinner than the near side (e.g. Dwek et al. 1995). For a distant galaxy, no such projection effects are present. However, extinction within an edge-on disk can play a similar role to that of distance in the Galaxy, and can help to constrain the orientation of a bar. If dust is present in significant amount, the spectroscopic signature of the far side of the bar in the PVDs should be fainter than that of the nearer side.

Figure 4.10 shows the surface density and PVDs of model 001 when considering a dust distribution proportional to the surface density of the gas (we take a constant absorption coefficient per unit mass κ; $\kappa = 0.1$ for Fig. 4.10). To illustrate the effects of the dust, we have decreased the surface densities in the surface density plot of Figure 4.10 to reflect the effective contribution of each point to the projected density at a viewing angle $\psi = 45°$. Unlike Figure 4.1, the PVDs are now far from symmetric with respect to the viewing angles $\psi = 0°$ and 90°. In addition, individual PVDs are no longer antisymmetric with respect to the center. This is mainly because the nuclear spiral obscures most of the material behind it, breaking the symmetry of the parallelogram-shaped signature of the x_1-like flow in the main and outer bar regions. For viewing angles $0° \lesssim \psi \lesssim 90°$, the nuclear spiral obscures mostly material moving away from the observer in the outer bar region, and obscures only a small amount of material moving toward the observer in the same region. Thus, the signature of the x_1-like flow in the PVDs is weakened for positive radial velocities, leading to a much fainter signature of the main and outer bar regions in the upper halves of the PVDs than in the lower halves. The opposite is true for viewing angles $90° \lesssim \psi \lesssim 180°$, where the signature of the main and outer bar regions is now much fainter in the lower halves. This effect is strongest and least extended for viewing angles of about 110° to 150°, as the line-of-sight is then parallel or at a small angle to the major axis of the nuclear spiral (which is slightly offset from that of the x_2 periodic orbits). Some effects

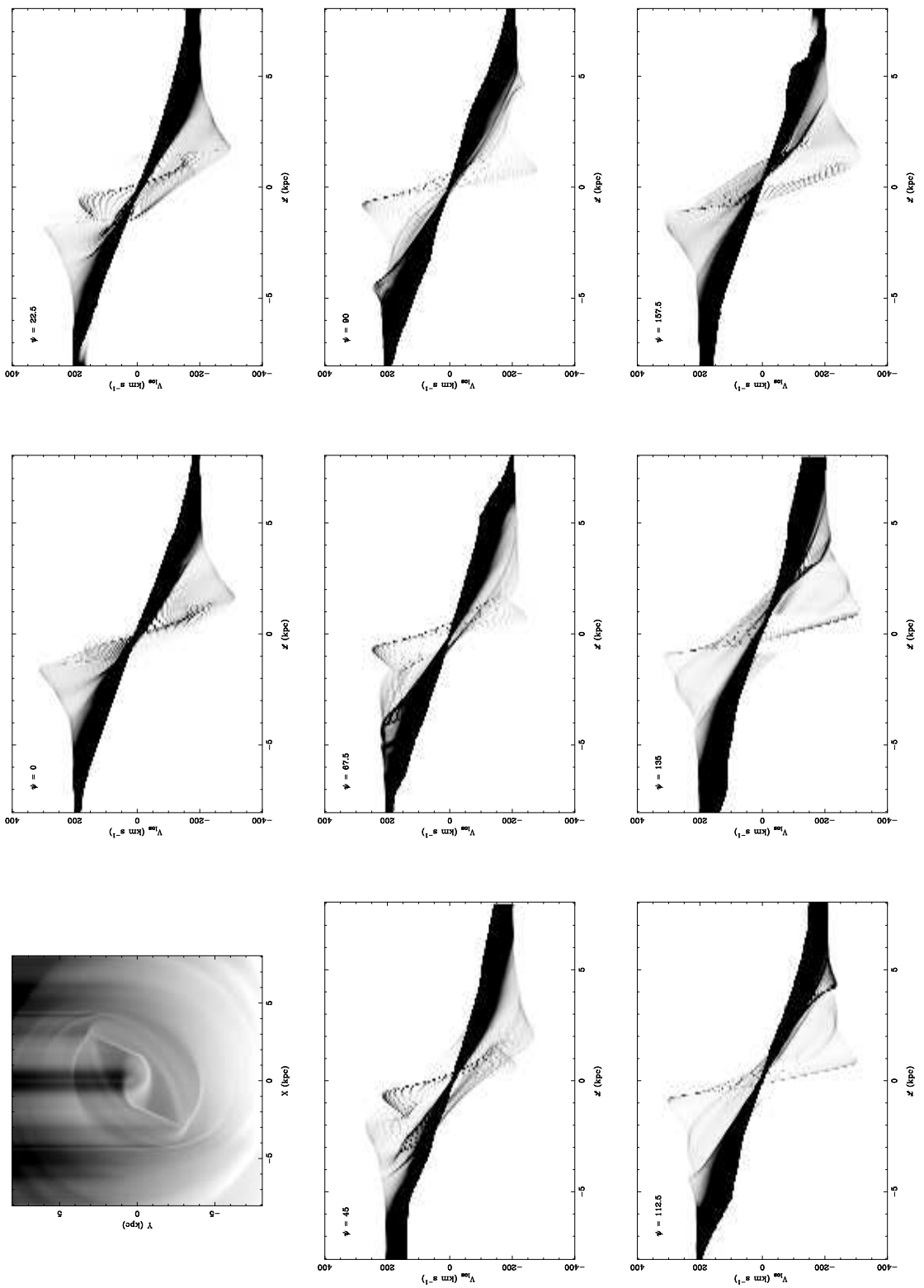

Figure 4.10: Same as Figure 4.1 but considering a dust distribution proportional to the gas surface density. The surface densities in the top-left plot have been decreased to reflect the effective contribution of each point to the integrated density along the line-of-sight for a viewing angle $\psi = 45°$. New features in the PVD for $\psi = 45°$ can thus be directly related to new features in the surface density plot.

on the signature of the nuclear spiral itself and on the signature of the outer parts of the simulation are present, but they are less pronounced.

In addition to the diagnostics suggested in the previous sections to identify a bar in an edge-on spiral galaxy, and determine whether it is seen end-on or side-on, the introduction of dust in the models has allowed us to develop criteria to determine in which half of the galaxy the near side of the bar is located. Of course, the distribution of dust in real galaxies will inevitably be more complex than the highly idealised distribution adopted here. Nevertheless, the features due to dust in the PVDs of Figure 4.10 can probably still be used as a guide to interpret asymmetries present in real data.

4.5 Discussion

Unlike periodic orbits studies (Kuijken & Merrifield 1995; Ch. 3), where one has to adopt a way of populating the orbits, hydrodynamical simulations provide both the density and the velocity of the gas. Furthermore, if some periodic orbit families intersect, it is not necessary to make a choice between them, since the simulations will reveal which family the gas follows in each region. Nevertheless, as we will discuss later in this section, the comparison with observations can still present some problems, since observations involve the strength of a given emission line rather than the gas density. Hydrodynamical simulations also make a number of approximations about the properties of the interstellar medium (ISM), and these may limit the applicability of the simulations to the interpretation of real data. We discuss such limitations for our simulations later on in this section as well.

Notwithstanding the problem of populating the orbits, there is generally a good agreement between the PVDs obtained from the periodic orbits approach in Chapter 3 and those obtained here from hydrodynamical simulations. This is because there are several similarities between the periodic orbits structure of the models and the gas flow (see A92b). We have in both cases a central component in the PVDs, which we identified in Chapter 3 with the x_2 orbits and in this chapter with the nuclear spiral. Further out, we have the domain of the x_1 orbits, which covers the main and outer regions of the bar in the simulations. In Chapter 3, by studying in detail the signatures of various periodic orbit families in the PVDs, we gained useful insight into the structure and kinematics of the gas from first principles. This allowed us to obtain a deeper understanding of the PVDs produced in the hydrodynamical simulations.

The main feature of the PVDs is the gap (fainter region), present at all viewing angles, between the signature of the nuclear spiral and that of the outer parts of the simulations. Such a structure would not be possible in an axisymmetric galaxy

and it can unmistakably reveal the presence of a bar or oval in an edge-on disk. This gap occurs because of the large-scale shocks which develop in the bar, driving an inflow of gas toward the center, and depleting the main and outer bar regions.

The gaps present in the PVDs produced with periodic orbits (see Kuijken & Merrifield 1995; Ch. 3) are different in nature from the ones observed here, being mainly due to the absence of populated orbits in certain regions of the models, particularly around corotation. As a result, the low density region extends well beyond corotation in these studies, although the exact extent depends on which orbits are neglected (e.g. as self-intersecting) and how the other orbits are populated. For example, in Figure 1 of Kuijken & Merrifield (1995), the gap extends to almost twice the corotation radius. We recall that three-dimensional N-body simulations of rotating disks produce bars which, when viewed edge-on, appear boxy-shaped if seen end-on and peanut-shaped if seen side-on (see, e.g., Combes & Sanders 1981; Combes et al. 1990; Raha et al. 1991). Taking the maximum height of the boxy/peanut-shaped bars to occur at half the corotation radius (Combes et al. 1990), we find that, in Kuijken & Merrifield's (1995) case, the ratio of the radial extent of the low density region of the PVDs to the radius where the maximum height of the peanut-shaped bulges occurs should be approximately 4 (associating the bulges with edge-on bars). On the other hand, in the hydrodynamical simulations presented here, the low density region of the PVDs reflects the low density region in the main and outer bar regions, and should thus be within corotation. When a bar is seen side-on, the ratio of the extent of the low density region to the radius of maximum height of the peanut-shaped bulge should thus be approximately 2. Kuijken & Merrifield (1995) report that this ratio is about 2 for the two galaxies they studied, in agreement with the prediction of our hydrodynamical simulations. These results can only be reconciled with the periodic orbits approach if the maximum height of the peanut-shaped bulges occurs near corotation (rather than halfway).

As we pointed out in § 4.3.2, the shape of the features present in the PVDs varies with the viewing angle, and can thus in principle be used to constrain the viewing angle to the bar in an observed galaxy. The envelope of the signature of the main and outer bar regions in the PVDs reaches very high radial velocities (compared to the outer parts of a simulation) for viewing angles close to the bar and relatively low velocities for viewing angles perpendicular to it. However, the envelope is so faint in most cases that it is unlikely to be of much use with real data (see § 4.3.4). The signature of the nuclear spiral has an inverted S-shape for $0^\circ \lesssim \psi \lesssim 90^\circ$ and is almost solid-body for $90^\circ \lesssim \psi \lesssim 180^\circ$. That feature is rather thick and does not show much fine structure, however, so it may be hard to use in conjunction with observations. The best viewing angle diagnostic is probably provided by the ratio of the maximum radial velocity reached by the nuclear spiral component and the velocity in the outer parts of a galaxy. This

ratio should be greater than unity for viewing angles perpendicular to the bar and smaller than unity for viewing angles parallel to it. Other properties of a PVD, such as the faintness of the signature of the main and outer bar regions, can also help to constrain the mass distribution and bar properties of an observed galaxy (see § 4.3.4). In practice, however, the analysis and modelling of spectroscopic data should not be a trivial task.

If a barred system has no nuclear spiral (or, equivalently, does not have an extended x_2 family of periodic orbits), there will not be a nuclear spiral component in the PVDs and no gap or double-peaked structure. An example of such a model was discussed in § 4.3.3. The only component likely to be detected observationally is then the solid-body signature of the outer parts of the galaxy. Thus, the kinematical detection of the presence of a bar is not straightforward. The first step would be to rule out such a slowly rising rotation curve (the rotation curve being defined as the upper limit of the envelope of an observed PVD), for example by calculating the shape of the rotation curve expected from the surface photometry. However, this would only show that the type of gas observed (ionised, H I, or molecular) is not present in sufficient quantities in the central region of the galaxy, but it would not provide any information on the cause of this depletion. It is thus probably necessary to use stellar kinematics to identify the bar in such systems. Because a large percentage of the stars in the central regions of barred disks are trapped around the x_1 orbits, there should be a clear bar signature in the stellar PVDs. We shall discuss the stellar kinematics and corresponding PVDs in Paper III. Let us note, however, that cases with no nuclear spiral component should be a minority, at least among strongly barred early-type spiral galaxies, since observational evidence argue that these systems possess ILRs (see, e.g., Athanassoula 1991; A92b). In particular, the fact that the dust lanes in most early-type strongly barred galaxies are offset along the leading sides of the bar, rather than centered and close to its major axis, is a strong argument for the existence of ILRs (A92b). Nevertheless, the existence of ILRs deserves further study, particularly for later type spirals. This can be done, for example, either by high resolution kinematical studies, to show the change of direction of the orbits or streamline ellipticities in the central parts of galaxies (e.g. Teuben et al. 1986), or by calculating the families of periodic orbits in galaxy potentials derived from observations, to show the existence or non-existence of the x_2 (and x_3) family.

Although our simulations cover a fair fraction of the available parameter space (see Table 1 in A92a), we have never come across a PVD showing a clear "figure-of-eight", as suggested by Kuijken & Merrifield (1995). In other words, the upper envelope of the low density region of the simulated PVDs is never as pronounced as it is in NGC 5746 or, to a lesser extent, in NGC 5965 and NGC 6722 (see Kuijken & Merrifield 1995; Fig. 5.1). By plotting the hydrodynamical PVDs with a logarithmic scale, or different grayscale levels, it is possible to show that, in some

cases, the upper envelope of the signature of the main and outer bar regions has a higher density than the rest of the signature at lower radial velocities. The effect, however, is never as strong as it is in NGC 5746. This feature thus needs further study. Somehow, these galaxies must be able to accumulate material at the ends of the bar on its *minor* axis. We note, however, that this feature is unusual. It is not present in most of the edge-on barred spiral galaxies identified in Chapter 5 (see Fig. 5.1).

Contrary to the "building blocks" approach of Chapter 3, which used combinations of periodic orbit families to model the structure and kinematics of barred galaxies, the hydrodynamical simulations presented here inherently take into account the collisional nature of gas, so the kinematics of the gaseous component of barred spirals is more accurately modelled. Approximations to the gas properties are nevertheless necessary, and we recall that the gas was treated as ideal, isothermal, infinitely thin, and non-self-gravitating. How much do our results depend on these assumptions, or, in other words, how model dependent are they?

The interstellar medium is a complicated multi-phase mixture, which can only be described schematically, particularly in non-local studies covering an object the size of a galaxy. Two different approaches have been developed so far. In the first one, the gas is treated as ballistic particles which, when they collide, loose energy according to pre-specified recipes (e.g. Miller, Prendergast, & Quirk 1970; Schwarz 1981, 1984; Combes & Gerin 1985). Unfortunately, the results of these simulations can depend on the adopted collision law (Guivarch & Athanassoula, in preparation), at least as far as the shocks in a barred region are concerned. The second approach is hydrodynamical, solving the Euler equations either with the help of a grid (e.g. van Albada & Roberts 1981; van Albada, van Leer, & Roberts 1982; Mulder 1986; Piner, Stone, & Teuben 1995), Smooth Particles Hydrodynamics (Lucy 1977; Gingold & Monaghan 1977; Hernquist & Katz 1989), or beams (Sanders & Prendergast 1974). A number of these studies assume an isothermal equation of state, following the model of Cowie (1980). He calculated the equation of state for an ensemble of clouds and found that it could be described as isothermal, provided the clouds have an equilibrium mass spectrum.

Comparing the results of all these schemes is beyond the scope of this paper. In all the approaches, the more reliable codes produce shocks in barred regions. Those shocks result in an inflow of gas and a substantial lowering of the density in the main and outer bar regions. However, the location, shape, and persistence of the shocks differ. Our main justification for adopting the present hydrodynamical code is that it gave good results in many previous studies (see A92b).

Since dissipation ensures that the gas layer in spiral galaxies remains thin, the two-dimensional nature of the simulations should not be a factor limiting the applicability of the results to the interpretation of real data. A further question

concerns the effect of self-gravity. Because our mass model represents best early-type barred spirals (see A92a), where the fraction of the total mass in gas is typically less than 10%, the contribution of the gas to the potential and large scale forces of real systems would be small. Lindblad, Lindblad, & Athanassoula (1996) found that including self-gravity in their model of NGC 1365 made very little difference to the global picture. It may well be, however, that locally, and in particular near high density structures such as the nuclear spiral, the self-gravity of the gas plays a role. This question should be explored in future work.

When using the bar diagnostics developed to interpret observational data, one has to take into account the fact that the PVDs were calculated using the gas *density* in the simulations and not the strength of a given gaseous emission line, which is what one usually observes. Physical conditions in the gas vary across the simulated disks, and will lead to different excitation mechanisms dominating in different parts of the disks. Regions of high density and low shear, such as the area around corotation, are likely to have higher star formation rates and thus more photoionised gas than elsewhere. Conversely, the gas in or near shocks, such as the nuclear spiral, will be mainly shock-excited (see Binette, Dopita, & Tuohy 1985; Dopita & Sutherland 1996), with possible star formation depending on the shear. Because different excitation mechanisms lead to different emission line ratios, the relative amplitudes of the various components of a PVD (e.g. the intensity of the signature of the outer parts of the disk versus that of the nuclear spiral) will depend on the emission line used in the observations. For example, we show in Chapter 5 that, for many objects, the signature of the nuclear spiral is very strong in the [N II] λ6548,6584 lines but is almost absent in the Hα line, probably indicating that it is shock-excited (the other components of the PVDs show [N II] λ6584/Hα ratios typical of H II regions). The PVDs were not corrected for stellar absorption, however, so these results should be interpreted with caution. Nevertheless, our PVDs should only be as guide when interpreting kinematical data. We stress that the morphology of the PVDs (the multiple components) is a more significant bar diagnostic than the distribution of intensity (the relative amplitudes of the components).

Similarly, under certain assumptions about the physical conditions in the gas, it is possible to use observed emission line ratios (e.g. Hα/Hβ) to measure the extinction due to dust. This could prove useful to interpret asymmetries in observed PVDs (see § 4.4 for a more complete discussion of likely dust effects).

4.6 Summary and Conclusions

Our main aim in this chapter, similarly to Chapter 3, was to develop diagnostics to identify bars in edge-on spiral galaxies, using the particular kine-

matics of the gaseous component of barred disks. To achieve this goal, we ran two-dimensional hydrodynamical simulations of the gas flow in the potential of a barred spiral galaxy mass model including a Ferrers bar, neglecting the self-gravity of the gas. We constructed position-velocity diagrams (PVDs) from those simulations using an edge-on projection and various viewing angles with respect to the major axis of the bar. The presence of shocks and inflows in the simulations allowed us to develop better bar diagnostics than those presented in Chapter 3.

We analysed in detail two simulations which are prototypes of simulations for models with and without inner Lindblad resonances (which we associate with the existence of x_2 periodic orbits). We showed that, for models allowing x_2 orbits, the nuclear spiral which is present in the center of the simulations produces a strong inverted S-shaped signature in the PVDs. This signature reaches high radial velocities (compared to those in the outer parts of the simulations) when the bar is seen side-on and relatively low velocities when the bar is seen end-on. The flow in the main and outer bar regions (the entire bar region if no nuclear spiral is present) produces a parallelogram-shaped signature in the PVDs, being associated with the x_1 periodic orbits. Because the flow is mostly parallel to the bar in that region, the highest velocities are now reached for viewing angles close to the bar major axis. In the outer parts of the simulations, the flow is almost circular and produces a strong almost solid-body signature in the PVDs for all viewing angles.

Shocks within the bar are present in most simulations and lead to a depletion of the gas in the region of the bar occupied by the x_1-like flow. Thus, if a nuclear spiral is present, a bar can easily be identified in an edge-on spiral galaxy, as there will be a gap in the PVD between the signature of the nuclear spiral and that of the outer parts of the galaxy. If there is no nuclear spiral, it may still be possible to detect a bar with the help of photometry and/or stellar kinematics. The envelope of the signature of the nuclear spiral, and to a lesser extent that of the main and outer bar regions, is most useful to determine the orientation of a bar with respect to the line-of-sight. Nevertheless, it is hard to discriminate between two viewing angles on either side of the bar. We showed that adding dust to the simulations helps break this degeneracy.

We also produced PVDs for a range of simulations covering most of the fraction of parameter space likely to be occupied by strongly barred early-type spiral galaxies. These simulations can be used to constrain the mass distribution and bar properties of an observed system. In particular, the presence or absence of the signature of a nuclear spiral in a PVD places strong constraints on the values our mass model parameters may take. The nuclear spiral can be absent for high bar axial ratios and/or bar quadrupole moments, and for low Lagrangian radii and/or central concentrations.

References

Athanassoula, E. 1991, in Dynamics of Disk Galaxies, ed. B. Sundelius (CTH: Göteborg), 149

———. 1992a, MNRAS, 259, 328 (A92a)

———. 1992b, MNRAS, 259, 345 (A92b)

Athanassoula, E., Bienayme, O., Martinet, L., & Pfenniger, D. 1983, A&A, 127, 349

Athanassoula, E., & Bureau, M. 1999, in preparation. (Paper III)

Beaulieu, S. F. 1996, Ph. D. Thesis, The Australian National University

Binette, L., Dopita, M. A., & Tuohy, I. R. 1985, ApJ, 297, 476

Binney, J., Gerhard, O., & Spergel, D. 1997, MNRAS, 288, 365

Binney, J., Gerhard, O. E., Stark, A. A., Bally, J., & Uchida, K. I. 1991, MNRAS, 252, 210

Combes, F., & Gerin, F. 1985, A&A, 150, 327

Combes, F., & Sanders, R. H. 1981, A&A, 96, 164

Combes, F., Debbasch, F., Friedli, D., & Sanders, R. H. 1990, A&A, 233, 82

Contopoulos, G. 1980, A&A, 81, 198

Contopoulos, G., & Papayannopoulos, T. 1980, A&A, 92, 33

Cowie, L. L. 1980, ApJ, 236, 868

de Carvalho, R. R., & da Costa, L. N. 1987, A&A, 171, 66

Dopita, M. A., & Sutherland, R. S. 1996, ApJS, 102, 161

Dwek et al. 1995, ApJ, 445, 716

Elmegreen, B. 1996, in Barred Galaxies, ed. R. Buta, D. A. Crocker, and B. G. Elmegreen (ASP: San Francisco), 197

Ferrers, N. M. 1877, Q.J. Pure Appl. Math., 14, 1

Gingold, R. A., & Monaghan, J. J. 1977, MNRAS, 181, 375

Hamabe, M., & Wakamatsu, K. 1989, ApJ, 339, 783

Hernquist, L., & Katz, N. 1988, ApJ, 349, 562

Kuijken, K., & Merrifield, M. R. 1995, ApJ, 443, L13

Kuzmin, G. 1956, AZh, 33, 27

Lindblad, P. A. B., Lindblad, P. O., & Athanassoula, E. 1996, A&A, 313, 65

Lucy, L. B. 1977, AJ, 82, 1013

Merrifield, M. R. 1996, in Barred Galaxies, ed. R. Buta, D. A. Crocker, and B. G. Elmegreen (ASP: San Francisco), 179

Miller, R. H., Prendergast, K. H., Quirk, W. J. 1970, ApJ, 161, 903

Mulder, W. A. 1986, A&A, 156, 354

Paczynski, B., Stanek, K. Z., Udalski, A., Szymanski, M., Kaluzny, J., Kubiak, M., Mateo, M., & Krzeminski, W. 1994, ApJ, 435, L113

Papayannopoulos, T., & Petrou, M. 1983, A&A, 119, 21

Piner, B. G., Stone, J. M., Teuben, P. J. 1995, ApJ, 449, 508

Raha, N., Sellwood, J. A., James, R. A., & Kahn, F. D. 1991, Nature, 352, 411

Sandage, A. 1961, The Hubble Atlas of Galaxies (Washington: Carnegie Institution)

Sanders, R. H., & Huntley, J. M. 1976, ApJ, 209, 53

Sanders, R. H., & Prendergast K. H. 1974, ApJ, 188, 489

Schwarz, M. P. 1981, ApJ, 247, 77

———. 1984, MNRAS, 209, 93

Sellwood, J. A. 1981, A&A, 99, 362

Sellwood, J. A., & Wilkinson, A. 1993, Re. Prog. Phys., 56, 173

Sevenster, M., Saha, P., Valls-Gabaud, D., & Fux, R. 1997, MNRAS, submitted.

Stanek, K. Z., Udalski, A., Szymanski, M., Kaluzny, J., Kubiak, M., Mateo, M., & Krzeminski, W. 1997, ApJ, 477, 163

Teuben, P., & Sanders, R. H. 1985, MNRAS, 201, 303

Teuben, P. J., Sanders, R. H., Atherton, P. D., & van Albada G. D. 1986, MNRAS, 221, 1

Toomre, A. 1963, ApJ, 138, 385

van Albada, G. D. 1985, A&A, 142, 491

van Albada, G. D., & Roberts, W. W. 1981, ApJ, 246, 740

van Albada, G. D., van Leer, B., & Roberts, W. W. 1982, A&A, 108, 76

Wada, K., Taniguchi, Y., Habe, A., & Hasegawa, T. 1994, ApJ, 437, L123

Weinberg, M. D. 1992, ApJ, 384, 81

Zao, H. S., Spergel, D. N., & Rich, R. M. 1994, AJ, 108, 2154